Satellite-based, top-down approach for the adjustment of aerosol precursor emissions over East Asia: TROPOMI NO₂ product, and the Geostationary Environment Monitoring Spectrometer (GEMS) AOD data fusion product and its proxy

5 Jincheol Park[1], Jia Jung[2], Yunsoo Choi[1*], Hyunkwang Lim[3], Minseok Kim[4], Kyunghwa Lee[5], Yungon Lee[6], Jhoon Kim[4,7]

[1]Department of Earth and Atmospheric Sciences, University of Houston, Houston, TX, USA
[2]Atmospheric Sciences and Global Change Division, Pacific Northwest National Laboratory (PNNL), Richland, WA, USA
[3]National Institute for Environmental Studies, Tsukuba, Japan
10 [4]Department of Atmospheric Sciences, Yonsei University, Seoul, South Korea
[5]Environmental Satellite Center, Climate and Air Quality Research Department, National Institute of Environmental Research (NIER), Incheon, South Korea
[6]Department of Atmospheric Sciences, Chungnam National University, Daejeon, South Korea
[7]Particulate Matter Research Institute, Samsung Advanced Institute of Technology, Suwon, South Korea

15 *Correspondence to*: Yunsoo Choi (ychoi6@uh.edu)

Abstract. In response to the need for up-to-date emissions inventory and the recent achievement of geostationary observations afforded by the Geostationary Environment Monitoring Spectrometer (GEMS) and its sister instruments, this study aims to establish a top-down approach for adjusting aerosol precursor emissions over East Asia. This study involves a series of TROPOMI NO₂ product, GEMS AOD data fusion product and its proxy product, and CTM-based inverse modeling
20 techniques. We begin by sequentially adjusting bottom-up estimates of nitrogen oxides (NO_x) and primary particulate matter (PM) emissions, both of which significantly contribute to aerosol loadings over East Asia, to reduce model biases in aerosol optical depth (AOD) simulations during the year 2019. While the model initially underestimates AOD by 50.73% on average, the sequential emissions adjustments that led to overall increases in the amounts of NO_x emissions by 122.79% and of primary PM emissions by 76.68% and 114.63% (single- and multiple-instrument-derived emissions adjustments,
25 respectively), reduce the extent of AOD underestimation to 33.84% and 19.60%, respectively. We consider the outperformance of the model using the emissions constrained by the data fusion product the result of the improvement in the quantity of available data. Taking advantage of the data fusion product, we perform sequential emissions adjustments during the spring of 2022, the period during which the substantial reductions in anthropogenic emissions took place accompanied by the COVID-19 pandemic lockdowns over highly industrialized and urbanized regions in China. While the model initially
30 overestimates surface $PM_{2.5}$ concentrations by 47.58% and 20.60% in the North China Plain (NCP) region and Korea, the sequential emissions adjustments that led to overall decreases in NO_x and primary PM emissions by 7.84% and 9.03%, respectively, substantially reduce the extent of $PM_{2.5}$ underestimation to 19.58% and 6.81%, respectively. These findings

indicate that the series of emissions adjustments, supported by TROPOMI and GEMS-involved data fusion products, performed in this study are generally effective at reducing model biases in simulations of aerosol loading over East Asia; in particular, the model performance tends to improve to a greater extent on the condition that spatiotemporally more continuous and frequent observational references are used to capture variations in bottom-up estimates of emissions. In addition to reconfirming the close association between aerosol precursor emissions and AOD as well as surface $PM_{2.5}$ concentrations, the findings of this study could provide a useful basis for how to most effectively exploit multi-source top-down information for capturing highly varying anthropogenic emissions.

1 Introduction

In East Asia, atmospheric aerosols, such as particulate matter (PM), have been a focus of great concern because of their adverse impact on public health and safety, accompanied by rapid urban and industrial growth that has elevated levels of anthropogenic emissions over time (Hatakeyama et al., 2001; Ohara et al., 2007). In response to the growing interest in airborne hazards, many research entities, using ground-based networks of monitoring sites in many industrial regions and megacities over East Asia, have devoted considerable effort to systemically monitoring local and regional air quality. Unfortunately, the limited number of stations often impedes efforts to secure efficient sampling coverage and data availability for aerosol studies (Kumar et al., 2007; Tian and Chen, 2010).

To overcome this limitation, many research entities have substantially improved the collection and, thus, the availability of satellite observational data, which enables them to estimate the spatiotemporal distributions of aerosols over vast areas that are not in close proximity to monitoring sites (Remer et al., 2013; Levy et al., 2013). A variety of aerosol products derived from sun-synchronous low Earth orbit (LEO) satellite instruments, such as the Advanced Very High Resolution Radiometer, the Visible Infrared Imaging Radiometer (VIIRS), the MODerate-resolution Imaging Spectroradiometer (MODIS), and the Multiangle Imaging SpectroRadiometer (MISR), have been available for many years (Chan et al., 2013; Ahn et al., 2014; Levi et al., 2015; Garay et al., 2020). For example, researchers have conducted a number of comprehensive air quality assessments on local to global scales using the aerosol optical depth (AOD), an essential property of aerosols that represents columnar aerosol loadings in the atmosphere (Bellouin et al., 2005; Remer et al., 2008, Munchak et al., 2013; Filonchyk et al., 2019; Jung et al., 2019, 2021; Lee et al., 2022).

Since the recent advent of satellite products, researchers have increased their efforts to use top-down observational data to improve the performance of chemical transport models (CTMs) such as the Community Multiscale Air Quality (CMAQ) model (Byun and Schere, 2006). A number of studies have applied satellite data in CTM-based numerical approaches, such as inverse modeling and data assimilation, to reduce the uncertainties in bottom-up estimates of air pollutant emissions and perform more accurate air quality simulations (Wang et al., 2012; Ku et al., 2013; Koo et al., 2015; Pang et al., 2018; Xia et al., 2019; Wang et al., 2020; Li et al., 2021; Lee et al., 2022); most of these studies, however, share a common challenge in

2

resolving uncertainties originating from retrieval discontinuity (i.e., coarse orbiting cycles of satellite instruments and cloud contamination). Using Ozone Mapping and Profiler Suite products, Wang et al. (2020) performed top-down optimizations of nitrogen dioxide (NO_2) and sulfur dioxide (SO_2) emissions and examined the sensitivity of AOD to concentrations of secondary inorganic aerosols over East Asia. Their results suggested a need for spatiotemporally more continuous satellite data. To improve model estimate of the AOD over East Asia, Li et al. (2021) used Ozone Monitoring Instrument data to perform a top-down inversion of SO_2 emissions. Their results emphasized the need for satellite data at finer temporal scales, which would allow one to capture highly variable SO_2 emissions over East Asia.

To address such instrument-inherent challenges, researchers have developed a number of approaches to applying more continuous and frequent observational data afforded by geostationary Earth orbit (GEO) satellite instruments; temporal resolutions of GEO satellite instruments (e.g., from a few minutes to an hour) are relatively finer than those of LEO satellite instruments on a 12-hour orbit cycle at best over given geographic locations (Vijayaraghavan et al., 2008). Leveraging aerosol product data derived from GEO satellite instruments such as the Geostationary Ocean Color Imager (GOCI) and the Advanced Himawari Imager (AHI), several CTM-based studies have shown substantial improvements in model performances in estimating aerosol loadings in East Asia (Jeon et al., 2016; Lee et al., 2016; Yumimoto et al. 2016; Jin et al., 2019). In addition, in response to the increasing demand for satellite data available at finer temporal resolutions, the Committee on Earth Observation Satellites has led an international effort to coordinate a new constellation of GEO satellite instruments for monitoring the behaviors of atmospheric constituents over the globe at faster sampling rates. For example, the Geostationary Environment Monitoring Spectrometer (GEMS), jointly developed by the Korea Aerospace Research Institute and Ball Aerospace, was launched onboard the GEO-KOMPSAT-2B satellite in 2020 as the first ultraviolet-visible (UV-Vis) instrument of its kind that can measure the columnar loadings of both trace gases and aerosols over the Asia-Pacific region in a geostationary manner up to eight times during daytime (Choi et al., 2018; Kim et al., 2018; Kim et al., 2020); before the advent of the GEMS mission, all UV-Vis instruments had been operating on LEO platforms. Furthermore, equipped with similar observational capabilities, a series of GEO satellite instruments are planned to be launched in 2023 to complete building the future constellation, which includes NASA's Tropospheric Emissions: Monitoring of Pollution (TEMPO) above North America (Zoogman et al. 2017) and the European Space Agency Sentinel-4 above Europe and North Africa (Ingmann et al., 2012), and ultimately serve the needs of more detailed and frequent air quality measurements over the Northern Hemisphere.

In addition to taking advantage of such finer spatiotemporal resolutions afforded by GEO satellite instruments, researchers have developed numerous data fusion approaches to integrating atmospheric properties retrieved by multiple individual instruments in order to further improve the quality of satellite products; the products derived from multiple instruments can be spatiotemporally complementary in terms of the completeness of observational data (Zou et al., 2020). For example, several studies have fused multi-source satellite products to yield more accurate estimates of air quality over East Asia (Choi

3

et al., 2019; Go et al., 2020; Lim et al., 2021) in response to the upcoming releases of GEMS products. Choi et al. (2019) fused multiple aerosol products afforded by three LEO satellite instruments (i.e., MODIS, MISR, and VIIRS) and two GEO satellite instruments (i.e., GOCI and AHI) to examine how effective the data fusion approach was at improving the accuracy of AOD estimates over East Asia. Their results showed that the multi-source aerosol product could substantially improve

100   observational coverage and frequency, and the AOD estimates from which showed closer spatiotemporal agreement with in situ ground-based measurements at AErosol RObotic NETwork (AERONET) sites (Holben et al., 1998) than those from AOD estimates provide by each of the individual satellite instruments (Choi et al., 2019). As a follow-up study over East Asia, Lim et al.' (2021) fused the GOCI AOD with AHI AOD (hereafter referred to as GOCI-AHI AOD) products by using multi-source aerosol properties and land surface parameters from those in ensemble-mean and maximum-likelihood

105   estimation (MLE) methods in order to reduce observational and systematic biases occurring during the retrieval process. Their multi-source AOD estimates showed substantially improved agreement with AERONET AOD measurements over East Asia, which they considered to be the result of complementary retrievals that reduced the number of pixels with missing values and ensured more cloud-free pixels (Lim et al., 2021). Note that their study aimed to develop and examine data fusion algorithms for near-future use, which would be applied to producing synergistic satellite products after the full product

110   releases of GEMS and its sister instruments, including the Advanced Meteorological Imager (AMI) onboard the GEO-KOMPSAT-2A satellite and Geostationary Ocean Color Imager 2 (GOCI-2) onboard the GEO-KOMPSAT-2B satellite.

Despite the availability of the many numerical approaches and data fusion techniques for reducing the uncertainties in the model and observations, efforts to couple them have not been sufficiently rigorous over East Asia; therefore, this study aimed to examine the utility of synergistic satellite observation data in improving the performance of CTM-based

115   simulations of aerosol loadings over East Asia. Hypothesizing that finer spatiotemporal resolutions of multi-source data fusion products would provide more observational references available for use, we employed the GEMS data fusion product and its proxy data in adjusting the emissions inventory in East Asia in a top-down manner. This study largely consists of two phases: 1) the implementation and evaluation of emissions adjustments using the TROPOspheric Monitoring Instrument (TROPOMI) tropospheric NO_2 columns (hereafter referred to as TROPOMI NO_2 columns), and AHI AOD and GOCI-AHI

120   fused AOD (the proxies of GEMS AOD and GEMS-AHI-GOCI-2 fused AOD, respectively) for the simulation year 2019, and 2) the application of the emissions adjustment approach using the TROPOMI NO_2 columns and GEMS-AHI-GOCI-2 fused AOD for the spring of 2022. For the former period, which represents the most recent year before the COVID-19 outbreak in this study, we first performed inverse modeling to constrain bottom-up estimates of nitrogen oxides (NO_x) emissions using TROPOMI NO_2 columns, and then we constrained bottom-up estimates of primary PM emissions using

125   each of the AHI AOD and GOCI-AHI fused AOD. Prior to proceeding with the second phase, we compared the model performances from using the single-instrument- and multi-source-derived AOD products in constraining primary PM emissions. For the latter period, which was considered to be severely affected by the resumptions of city- and province-wide lockdowns (Dyer, 2022) in China, we used the TROPOMI NO_2 columns and GEMS-AMI-GOCI-2 fused AOD to

4

sequentially constrain NO_x and primary PM emissions based on the earlier top-down approach. Note that we did not focus on

130   other gaseous air pollutants than NO_x considering the future application of GEMS tropospheric NO_2 product, which has recently been released (as of November 23, 2022) by Environmental Satellite Center of Korean National Institute of Environmental Research (NIER) (https://nesc.nier.go.kr). And then, using a series of a posteriori emissions (i.e., NO_x-constrained emissions and NO_x- and primary PM-constrained emissions) in CMAQ, we simulated AOD and $PM_{2.5}$ concentrations over East Asia to examine the utility of the GEMS-involved synergistic product in inverse modeling and

135   ultimately to improve model performances in estimating aerosol loadings over East Asia.

2 Materials and Methods

2.1 Modeling setup and preparation of base emissions

Using the 2016 KORUS-AQ emissions inventory version 5.0 developed by Konkuk University (Woo et al., 2020), we prepared CMAQ-ready anthropogenic emission inputs over the modeling domain, shown in Fig. 1, which encloses the

140   eastern half of China, the Korean Peninsula, southern Russian Far East, and Japan. The KORUS-AQ emissions inventory consists of multiple individual emissions inventories, including the Comprehensive Regional Emissions for Atmospheric Transport Experiments version 2.3 (Jang et al., 2019), Clean Air policy Support System 2015 (Yeo et al., 2019), and Studies of Emissions and Atmospheric Composition, Clouds, and Climate Coupling by Regional Surveys (Toon et al., 2016). To prepare biogenic emissions inputs, we employed the Model of Emissions of Gases and Aerosols from Nature (MEGAN)

145   version 3.0 (Guenther et al., 2012), which can speciate, quantify, and regrids biogenic emissions from terrestrial ecosystems based on a series of input data (e.g., meteorological fields and land surface parameters) (Guenther et al., 2006, 2020). We used reprocessed MODIS version 6 leaf area index (LAI) products (Yuan et al., 2011) and VIIRS global green vegetation fraction (GVF) products (Jiang et al., 2016) as input data for MEGAN. We merged the anthropogenic and biogenic emissions to prepare the a priori emissions inputs (hereafter referred to as base emissions).
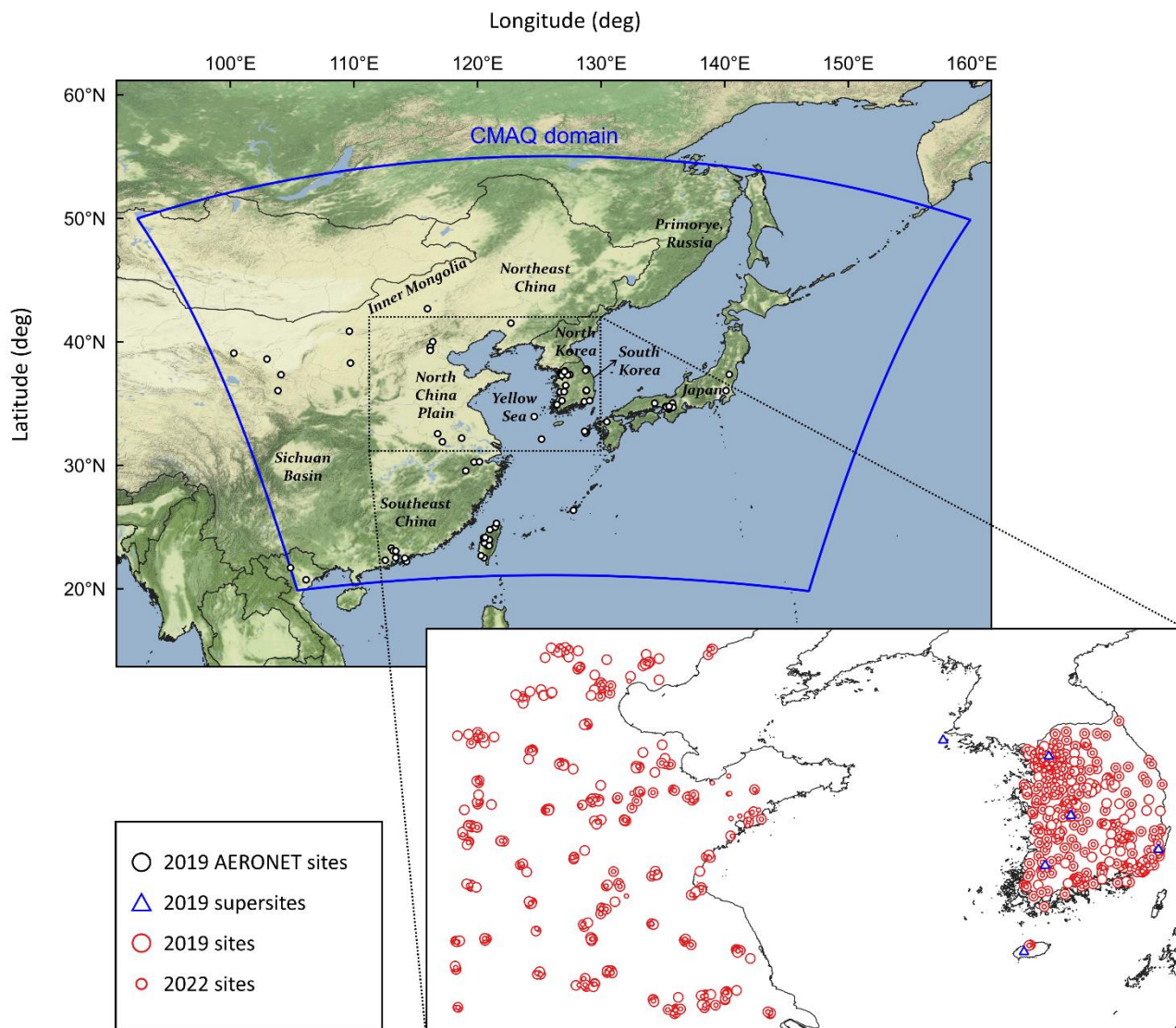
Figure 1. Modeling domain and the locations of the ground-based in-situ measurement sites used for model evaluation. AERONET sites are presented in the upper panel, and the rest of air quality monitoring sites are in the below.

To simulate the meteorological fields and ambient concentrations of gaseous air pollutants and aerosols for each of the study periods, we used the Weather Research and Forecasting (WRF) version 3.8 developed by the National Center for Atmospheric Research (NCAR) (Skamarock et al., 2008) and CMAQ version 5.2 developed by the U.S. Environmental

Protection Agency (EPA) (Byun and Schere, 2006). Employing the same modeling setups and initial conditions used in our previous studies over East Asia (Jung et al., 2019, 2021; Pouyaei et al., 2020, 2021; Park et al., 2022), we configured WRF and CMAQ to cover the modeling domain at a horizontal resolution of 27 km and 35 vertical variable thickness layers from the surface up to 100 hPa. Detailed model configurations are listed in Table S1. Then, using the WRF-simulated meteorological fields and base emissions in CMAQ, we simulated NO_2 columns and concentrations, AOD, and $PM_{2.5}$ concentrations over the modeling domain for the entire year 2019 and the period from March to May 2022. For each of these two study periods, we initiated both WRF and CMAQ simulations with a 10-day spin-up time.

2.2 TROPOMI NO₂ product

TROPOMI, an LEO satellite instrument launched onboard the Copernicus Sentinel-5 Precursor satellite in 2017, provides global observations of trace gases and aerosols (Veefkind et al., 2012). To obtain daily tropospheric NO_2 and SO_2 column densities observed during the study periods, we used TROPOMI Level 2 NO_2 and SO_2 products. The spatial resolution of TROPOMI was initially 3.5 km × 7 km and was improved to 3.5 km × 5.5 km in early August 2019. The daily acquisition time of the column data was approximately 04:30 UTC when the instrument overpassed the modeling domain during the study period. For the NO_2 columns, we used pixels with quality assurance values (qa_values) larger than 0.75 and cloud fractions smaller than 0.3. To ensure consistency in the horizontal spacings between the TROPOMI NO_2 columns and CMAQ's modeling grids, we regridded the TROPOMI NO_2 columns into 27 km × 27 km grids by using distance-weighted mean of those observation references with a radius of 0.25° (approximately 27 km).

2.3 AHI AOD and GOCI-AHI fused AOD products

The AHI, a GEO satellite instrument launched onboard the Himawari-8 geostationary meteorological satellite in 2014, provides regional observations of aerosol properties over East Asia and western Pacific regions in a spatiotemporally continuous manner (Okuyama et al., 2015; Bessho et al., 2016). For the study period 2019, we used the Japan Aerospace Exploration Agency (JAXA) AHI Level 3 aerosol product to obtain the hourly estimates of AOD over the modeling domain, the spatiotemporal resolutions of which are 0.05° × 0.05° and one hour for 8 consecutive daytime (00:30 UTC to 07:30 UTC) retrievals per day. To ensure consistency between the observed AOD and modeled AOD, the latter of which was estimated based on the light extinction of aerosols at a wavelength of 550 nm (Pitchford et al., 2007), we converted the AHI AOD retrieved at 500 nm wavelength to those at a 550 nm wavelength following Eq. 1 (Angstrom, 1961):

$$AOD_{550\,nm} = AOD_{500\,nm} \times \left(\frac{550}{500}\right)^{-AE} \qquad (1)$$

where $AOD_{550\,nm}$ and $AOD_{500\,nm}$ are AODs at 550 and 500 nm wavelengths, respectively, and AE is the Angstrom exponent at 400 - 600 nm wavelengths provided in the AHI aerosol product. To ensure the retrieval quality, we used pixels with quality assurance values (AOT_merged_uncertainty) smaller than 1 (very good and good retrievals).

7

To explore the utility of the synergistic observational data in the emission adjustments, we employed the GOCI-AHI fused AOD product developed by Lim et al. (2021), which provides near-real-time bias-corrected AOD estimates over East Asia, taking advantage of multi-source retrievals of aerosol optical properties that complement each other. GOCI, a GEO satellite instrument launched onboard the Communication, Ocean and Meteorological Satellite (COMS-1) in 2010, provides regional observations of ocean environments (i.e., sea surface albedo and reflectance) and aerosol properties (i.e., the AOD) over East Asia and western Pacific regions (Lee et al., 2010). The GOCI-AHI AOD product affords the best compromise among four individual retrievals post-processed based on Yonsei Aerosol Retrieval (YAER) retrieval algorithms (Choi et al., 2016, 2018; Lim et al., 2018); the data fusion process comprises a series of post-processing and data fusion techniques to complement the error characteristics of each other (i.e., the spatiotemporal collocation, the cloud removal process, the ensemble-mean method, the MLE method, and systematic bias correction based on the long-term validation of AERONET AOD measurements) (Lim et al., 2021). For the study period 2019, we used the GOCI-AHI fused AOD product to obtain hourly estimates of the AOD (at a 550 nm wavelength) over the modeling domain, the spatial resolution of which was initially 6 km $\times$ 6 km and regridded into $0.05° \times 0.05°$, and the temporal resolution of which is identical to that of the AHI AOD product described above. The consistency in the grid spacings among AHI AOD, GOCI-AHI AOD, and CMAQ's modeling grids was ensured in the same approach described in Section 2.2 above.

2.4 GEMS-AMI-GOCI-2 fused AOD product

The GEMS-AMI-GOCI-2 fused AOD product is a synergistic science product jointly developed by Yonsei University, Chungnam National University, and the Korean National Institute of Environmental Research (NIER) based on their earlier data fusion approach applied to the GOCI-AHI fused AOD product (the proxy of the GEMS-AMI-GOCI-2 fused AOD product in this study) described in Sect. 2.3. GEMS provides hourly daytime observations of the columnar loadings of gaseous air pollutants (i.e., ozone, NO_2, SO_2, formaldehyde, and glyoxal) and aerosols (i.e., the AOD) (Kim et al., 2020a). The AMI, a meteorological satellite instrument, provides regional observations of meteorology (i.e., cloud mask) and terrestrial environments (i.e., vegetation indices, surface reflectivity, albedo, and turbid water) as well as aerosol optical properties (i.e., fine mode fraction (FMF) and AOD) every 10 minutes at spatial resolutions of 0.5 km - 1.0 km for visible channels and of 2 km for near-infrared and infrared channels (Chung et al., 2020; Kim et al., 2021). GOCI-2, an advanced ocean color imager that succeeded the mission of GOCI, provides hourly observations of ocean environments (i.e., ocean current, green tide, and red tide) as well as of aerosol optical properties (i.e., FMF and AOD) over the ocean surface at a full-domain spatial resolution of 1 km (Kim et al., 2020a). Note that these three individual instruments are in operation onboard two sister GEO platforms (i.e., the AMI onboard GEO-KOMPSAT-2A, and GEMS and GOCI-2 onboard GEO-KOMPSAT-2B) over the Asia-Pacific region. To create the best synergy from the superiorities of these instruments over each other (i.e., GEMS's retrieval accuracy over bright surfaces, and AMI's and GOCI-2's sampling performances over cloud-free pixels at finer spatiotemporal resolutions) (Kim et al., 2020b), the data fusion process utilizes GEMS Level 2 aerosol product version 1, and AMI and GOCI-2 aerosol products post-processed based on the YAER algorithm (Kim et al., 2020b) to produce the

GEMS-AMI-GOCI-2 AOD product. For the study period 2022, we used the GEMS-AMI-GOCI-2 AOD product to obtain the hourly estimates of AOD (at a 550 nm wavelength) collocated into the spatiotemporal resolutions identical to those of the AHI AOD and GOCI-AHI AOD products described earlier. Detailed information about the data fusion process is provided by Kim et al. (2020b).

2.5 Top-down approaches for NOₓ and primary PM emissions adjustments

2.5.1 Emissions adjustments for the study period 2019

To constrain the NO_x and primary PM emissions based on top-down information provided by satellite instruments for the study period 2019, we employed a series of inverse modeling techniques. To adjust the a priori NO_x emissions, we performed analytical (or Bayesian) inverse modeling towards mathematically minimizing the difference between TROPOMI NO_2 and CMAQ-simulated NO_2 columns based on the following cost function in Eq. 2 under the assumptions that 1) the relationship between the changes in NO_2 columns and NO_x emissions is not rigorously nonlinear, 2) observation and emission error covariances are described by zero-bias Gaussian probability density functions, and 3) observation and emission error covariances are independent of each other (Rodgers, 2000):

$$J(x) = \frac{1}{2}\left(y - F(x)\right)^T S_o^{-1}\left(y - F(x)\right) + \frac{1}{2}(x - x_a)^T S_e^{-1}(x - x_a) \qquad (2)$$

where x is a posteriori NO_x emissions, x_a a priori NO_x emissions, S_o the observational error covariance provided in the TROPOMI NO_2 product, and S_e the error covariance of the a priori NO_x emissions, the uncertainty of which was calculated by combining the error covariances of anthropogenic (50%) and biogenic (200%) NO_x emissions (Souri et al., 2020; Jung et al., 2022). F is the first-order sensitivity coefficient that correlates NO_x emissions with tropospheric NO_2 columns. We used the CMAQ decoupled direct method in three dimensions (CMAQ DDM-3D) version 5.2 (Napelenok et al., 2006) to compute the initial sensitivity coefficient, a measure of the responses of modeled NO_2 columns to changes in NO_x emissions. We used the same model configurations in CMAQ DDM-3D as those used in CMAQ described in Sect. 2.1. To infer the a posteriori emissions, we used the Gauss-Newton method in Eq. 3 (Rodgers, 2000):

$$x_{i+1} = x_a + S_e K_i^T (K_i S_e K_i^T + S_o)^{-1}[y - F(x_i) + K_i(x_i - x_a)] \qquad (3)$$

where i is the number of iteration, and K is the Jacobian matrix calculated in CMAQ DDM-3D. We iterated Eq. 3 two times within each month to attain convergence, and F and K were updated after each iteration. It should be noted that we derived $\log(x)$ instead of x to constrain negative a posetriori values, the details of which are described in Souri et al. (2018). And then, we applied the monthly emissions adjustment ratios derived from Eqs. 2 and 3 to the base emissions to update the bottom-up estimates of NO_x emissions over the modeling domain (hereafter referred to as 2019 NO_x-constrained emissions).

Further details about the analytical inverse modeling approach employed in this study are provided by Souri et al. (2020) and Jung et al. (2022).

To adjust the primary PM emissions, we applied analytical inversion described in Eqs. 2 and 3 to the emissions of 19 primary PM species predefined as contributors to the AOD in the 6th generation CMAQ aerosol module (AERO6) (Simon, 2015) listed in Table S2. Note that the primary PM emissions, hereafter, refer to the summation of the emissions of all 19 individual primary PM species. In Eq. 2, x is a posteriori primary PM emissions, x_a is a priori primary PM emissions (in the NO_x-constrained emissions inventory obtained earlier), and S_e the error covariance of the a priori primary PM emissions, the uncertainty of which was set as 100% (Crippa et al., 2019). For S_o, we employed $\pm 0.1 + 0.3 \times AOD$ (Zhang et al., 2020) and $\pm 0.043 + 0.178 \times AOD$ (Lim et al., 2021) as the observational error covariances of the AHI AOD and the GOCI-AHI AOD, respectively. To compute F, since CMAQ DDM-3D is not available for aerosols, we employed the brute-force method (BFM) described in Eq. 4 (Napelenok et al., 2006):

$$F^{bfm} = \frac{C^{+10\%} - C^{-10\%}}{0.2} \qquad (4)$$

where F^{bfm} is the approximate first-order sensitivity coefficient that correlates primary PM emissions to the AOD, $C^{+10\%}$ the CMAQ-simulated AOD of the primary PM emissions perturbed by +10%, and $C^{-10\%}$ the CMAQ-simulated AOD of the primary PM emissions perturbed by -10%. In this approach, F^{bfm} represents the sensitivity of the total primary PM emissions with regard to changes in the AOD; therefore, the resultant adjustment ratio was applied to the emissions of each of the primary PM species equally, not in a selective manner due to the limited data availability. Note that no routine observations have been made until today for the loadings of such species over vast areas in East Asia in a top-down manner. We applied the daily emissions adjustment ratios derived from Eqs. 2, 3, and 4 to the 2019 NO_x-constrained emissions to update the bottom-up estimates of primary PM emissions over the modeling domain (hereafter referred to as 2019 NO_x- and PM-constrained emissions). To evaluate the model performance before and after the application of the sequential emission adjustments, we used the series of a priori and a posteriori emissions (i.e., the base emissions, 2019 NO_x-constrained emissions, and a pair of 2019 NO_x- and PM-constrained emissions using the AHI AOD and GOCI-AHI AOD) to perform CMAQ simulations for the study period 2019. It should be noted that NO_x emissions were adjusted monthly, due to the relatively coarse temporal resolution of TROPOMI NO_2 columns (providing zero to one valid snapshot of columnar NO_2 per day over the modeling domain), while primary PM emissions were adjusted daily by using the AOD products at sufficiently fine temporal resolutions afforded by geostationary platforms.

2.5.2 Emissions adjustments for the study period 2022

Similar to the approach described in Sect. 2.5.1, we first adjusted NO_x emissions by using the TROPOMI NO_2 columns obtained for the study period 2022 prior to proceeding with the primary PM emissions adjustment. To adjust the a priori NO_x emissions, we employed the basic mass balance method described by Martin et al. (2003) and Cooper et al. (2017). Assuming a direct linear relationship between changes in both the NO_2 columns and the NO_x emissions, we adjusted the a priori NO_x emissions based on the ratios between the TROPOMI NO_2 and CMAQ-simulated NO_2 columns following Eq. 5:

$$E_{2022} = \frac{E_{2019}}{\Omega_{2019}} \times \Omega_{2022} \qquad (5)$$

where E_{2022} represents the a posteriori NO_x emissions, E_{2019} the a priori NO_x emissions (from the 2019 NO_x-constrained emissions described in Sect. 2.5.1), Ω_{2019} and Ω_{2022} the TROPOMI NO_2 columns obtained for the study periods 2019 and 2022, respectively. We then applied the monthly emissions adjustment ratios derived from Eq. 5 to the 2019 NO_x-constrained emissions to update the NO_x emissions for the study period 2022 (hereafter referred to as 2022 NO_x-constrained emissions).

Then, to adjust the primary PM emissions, we used the GEMS-AMI-GOCI-2 AOD obtained for the study period 2022 to perform the analytical inversion and BFM described in Sect. 2.5.1 by using the S_o of $\pm (-0.001 + 0.48 \times AOD)$ provided in the GEMS-AMI-GOCI-2 AOD product and the perturbed ($\pm10\%$) primary PM emissions. The daily emissions adjustment ratios were applied to the 2022 NO_x-constrained emissions to update the primary PM emissions (hereafter referred to as 2022 NO_x- and PM-constrained emissions). Using the base emissions, 2022 NO_x-constrained emissions, and 2022 NO_x- and PM-constrained emissions to perform CMAQ simulations for the study period 2022, we evaluated the performance of the model

2.6 Ground-based measurements for model evaluation

To evaluate the model performance, we used ground-based in situ observations across South Korea (hereafter referred to as Korea) and the North China Plain (NCP) region. To validate the accuracy of the WRF-simulated meteorological fields, we obtained hourly measurements of the 2 m air temperature and 10 m wind U and V components from the Korean Meteorological Administration database (132 sites for 2019 and 95 for 2022). The WRF-simulated hourly meteorological fields showed fair agreements with the in situ measurements (Figures S1 and S2; Table S3), which we considered sufficient for further use as meteorological inputs for CMAQ.

To evaluate the performance of the CMAQ model, we obtained the hourly measurements of surface NO_2 and $PM_{2.5}$ concentrations from the AirKorea website (https://www.airkorea.or.kr) (346 sites for 2019 and 425 for 2022) and from the Chinese Ministry of Ecology and Environment database (MEE) (235 sites for 2019 and 312 sites for 2022), and hourly sun photometer measurements of the AOD (at a 550 nm wavelength) (85 AERONET sites for 2019). To ensure the quality of the

11

validation sets, we excluded observation sites in which the frequency of missing values exceeded 50% of all observations made during the study period. For the measurements collected from the MEE sites, we applied the quality assurance processes (e.g., elimination of negative values) that we used in our previous study over mainland China (Mousavinezhad et al., 2021). To quantify the extent of model overestimation and underestimation, we employed a normalized mean bias (NMB) following Eq. 6:

$$Normalized\ mean\ bias\ (NMB) = \frac{\sum_{i=1}^{n}(M_i - O_i)}{\sum_{i=1}^{n}(O_i)} \qquad (6)$$

where M represents the model predictions, O the observations, and n the total number of pairs.

To discuss the success of the sequential NO_x and primary PM emissions adjustments described in Sect. 2.5, we obtained the seasonal compositions of surface $PM_{2.5}$ assessed at six ground-based supersites in Korea, the constituents of which include secondary inorganic aerosols (i.e., nitrate, sulfate, and ammonium aerosols), organic carbon (the total mass of both primary and secondary organic carbon), elemental carbon, the lumped summation of other PM species listed in Table S2, and the rest remaining undefined (the lumped summation of all unidentified species in 2.5 microns or less in diameter, which still constitute the total $PM_{2.5}$ mass). The locations of the supersites are as follows: Incheon (37.61°N, 126.93°E), Seoul (37.96°N, 124.63°E), Daejeon (35.23°N, 126.85°E), Gwangju (36.32°N, 127.41°E), Ulsan (35.58°N, 129.32°E), and Jeju (33.35°N, 126.39°E).

3. Results and Discussions

3.1 Evaluation of the top-down approach using TROPOMI NO_2, AHI AOD, and GOCI-AHI AOD

We performed a series of emissions adjustments by using the TROPOMI NO_2 columns, AHI AOD, and GOCI-AHI AOD as the constraints to updating the bottom-up estimates of NO_x and primary PM emissions over the modeling domain. Prior to proceeding with the primary PM emissions adjustments, we examined the model performances in simulating NO_2 columns during the study period 2019 on a seasonal basis. The model using the base emissions tended to underestimate NO_2 columns over the major portion of the modeling domain during the entire study period (Figure S3). After the NO_x emissions adjustment, which resulted in overall increases in NO_x emissions by 71.64% - 174.16% (Figure S4; Table S4), the modeled NO_2 columns showed closer spatial agreements to the observed NO_2 columns (Figure S5). Then we evaluated the model performances in simulating daily surface NO_2 concentrations at ground-based in-situ measurement sites in Korea and the NCP region in a time series. Overall, the NO_x emissions adjustment led to a closer temporal agreement between the modeled and observed NO_2 concentrations with reduced model biases. While the model using the base emissions showed NMBs (Rs) of -24.20%, 15.63%, -2.06%, and -23.54% (0.66, 0.45, 0.72, and 0.71) in the spring, summer, fall, and winter, respectively, the model using the NO_x-constrained emissions showed NMB of -5.66%, 1.83%, 21.66%, and 13.45% (0.72, 0.63, 0.82, and

0.76) in the corresponding seasons, the results of which indicate that the NO_x emissions adjustment was effective (Figure S6; Table S5) at reducing the model biases in most seasons. However, in the NCP region, the NO_x emissions adjustment showed mixed results in reducing the model biases. While the model using the base emissions showed NMBs (Rs) of -13.90%, 5.25%, -11.43%, and -1.05% (0.75, 0.54, 0.50, and 0.55) in the spring, summer, fall, and winter, respectively, the model using the NO_x-constrained emissions showed NMBs of 12.34%, 22.32%, 15.24%, and 33.75% (0.75, 0.52, 0.55, and 0.59) in the corresponding seasons. Although the NO_x emissions adjustment led to some improvements in Rs in the NCP region, NMBs showed increases in the summer, fall, and winter seasons, which indicate that the emissions adjustment was not as effective in reducing the model biases in the NCP region as it was in Korea.

In addition to the NO_x emission adjustment, we performed primary PM emission adjustments followed by evaluating the model performance in simulating AOD during the study period 2019. To compare the use of the single-instrument- and multi-source-derived AOD products for constraining primary PM emissions, we performed two separate emission adjustments, using each of the AHI AOD and GOCI-AHI AOD as a constraint to updating the primary PM emissions over the modeling domain. To ensure the consistency between the comparisons, we spatially collocated the CMAQ-simulated AOD to each of the AHI AOD and GOCI-AHI AOD. We found that during the entire study period, the model using the base emissions tended to underestimate AODs over a major portion of the modeling domain except for a few inland regions in China (Figures 2a, 2b, 3a, and 3b). After the NO_x emissions adjustment, the modeled AODs showed closer spatial agreement with the observed AODs in Korea and the NCP region (Figures 2c and 3c); the model, however, tended to overestimate the AODs in some inland regions such as southeast China and the Sichuan Basin region; we consider this tendency the result of uncertainty in the bottom-up estimates of air pollutant emissions coming from the unique basin landform that often encloses highly concentrated anthropogenic emissions (Chen et al., 2021). After the primary PM emission adjustments using the AHI AOD and GOCI-AHI AOD, which resulted in overall increases in primary PM emissions by 19.55% - 31.79% (Figure S7; Table S6) and 87.54% - 142.96% (Figure S8; Table S6), respectively, the modeled AODs showed even closer spatial agreement with the observed AODs (Figures 2d and 3d).

We then evaluated the performance of the model at simulating daily mean AODs at AERONET sites in time series and found that overall, the series of emissions adjustments resulted in improvements in the performance of the model during the entire study period 2019. In brief, the model's initial underestimation of AOD was mitigated by the NO_x emissions adjustment, which led to increased NO_x emissions, and then by the subsequent primary PM emissions adjustment, which resulted in overall increases in primary PM emissions. Whereas the model using the base emissions showed an average NMB of -50.73% (Figure 4a; Table 1a), the model using the 2019 NO_x-constrained emissions showed an average NMB of -42.52% (Figure 4b; Table 1b). The model using the 2019 NO_x- and PM-constrained emissions showed average NMBs of -33.84% (using the AHI AOD) and -19.60% (using GOCI-AHI AOD), respectively (Figures 4c and 4d; Tables 1c and 1d). These results indicate that the sequential adjustments of NO_x and primary PM emissions were generally effective at

13

improving model performance in simulating the AOD; in particular, the use of the multi-source AOD product led to a greater reduction in model biases than that of the single-instrument AOD product. Despite the success of the sequential adjustments of NOx and primary PM emissions in improving the model's AOD simulations, there are still uncertainties remaining regarding the accuracy of NO_x emissions. For example, in the NCP region, the NO_x emissions adjustment caused the model to overestimate surface NO_2 concentrations in some seasons, and consequently, increased the model biases. Nevertheless, this overestimation was shown to help the model to reduce its AOD underestimation. Addressing this issue requires the development of region-specific tactics for adjusting the bottom-up estimates of gas-phase air pollutant emissions in future studies.
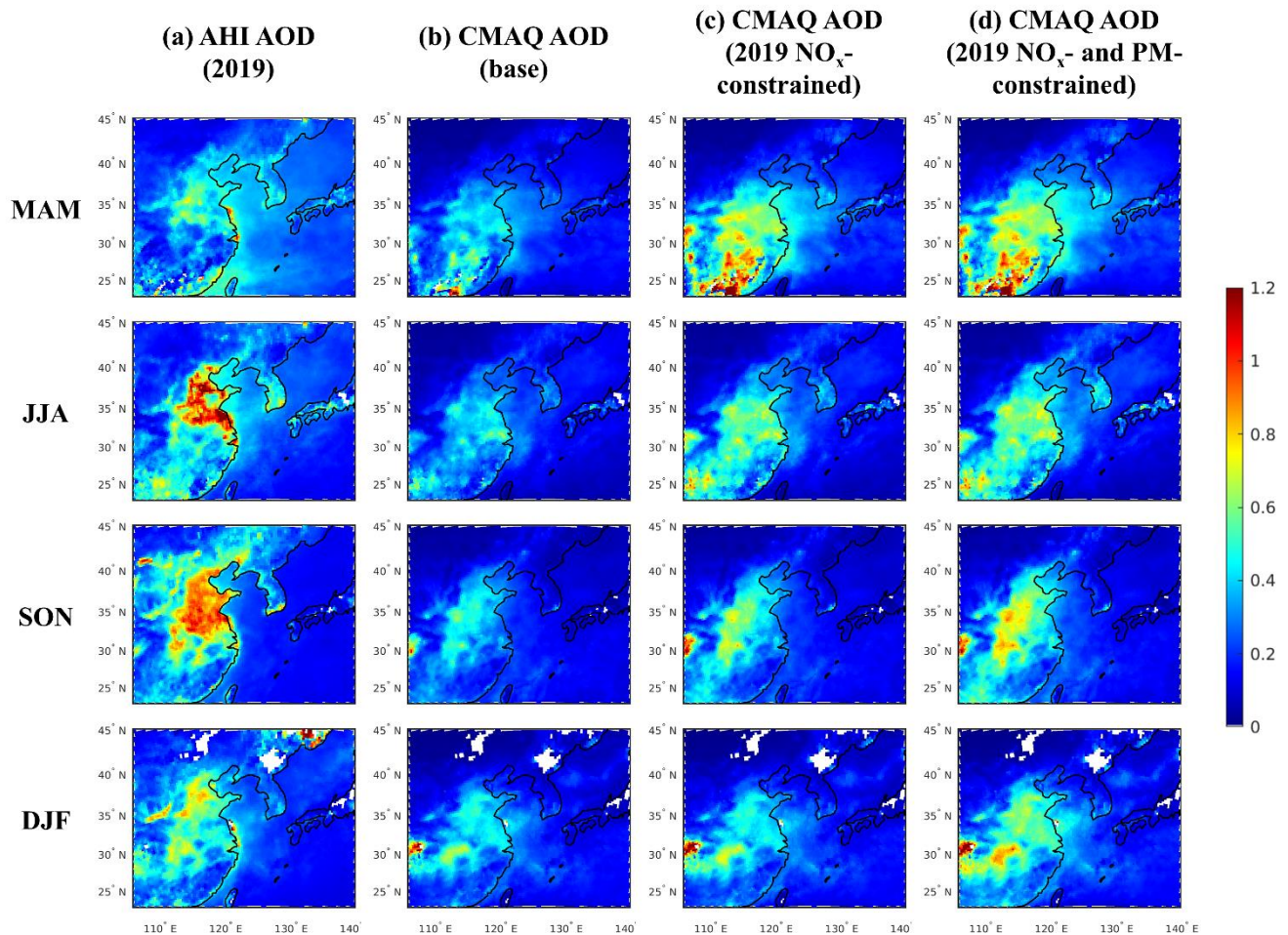
Figure 2. Spatial distributions of the AHI and CMAQ-simulated AODs before and after the NO_x emissions adjustment (based on TROPOMI NO_2 columns) and primary PM emissions adjustment (based on AHI AOD) during the study period 2019. (a) The AHI

AOD, (b) the CMAQ-simulated AOD using base emissions, (c) the CMAQ-simulated AOD using 2019 NO$_x$-constrained emissions, and (d) the CMAQ-simulated AOD using 2019 NO$_x$- and PM-constrained emissions. Note that CMAQ-simulated AODs were temporally collocated to the AHI AOD.
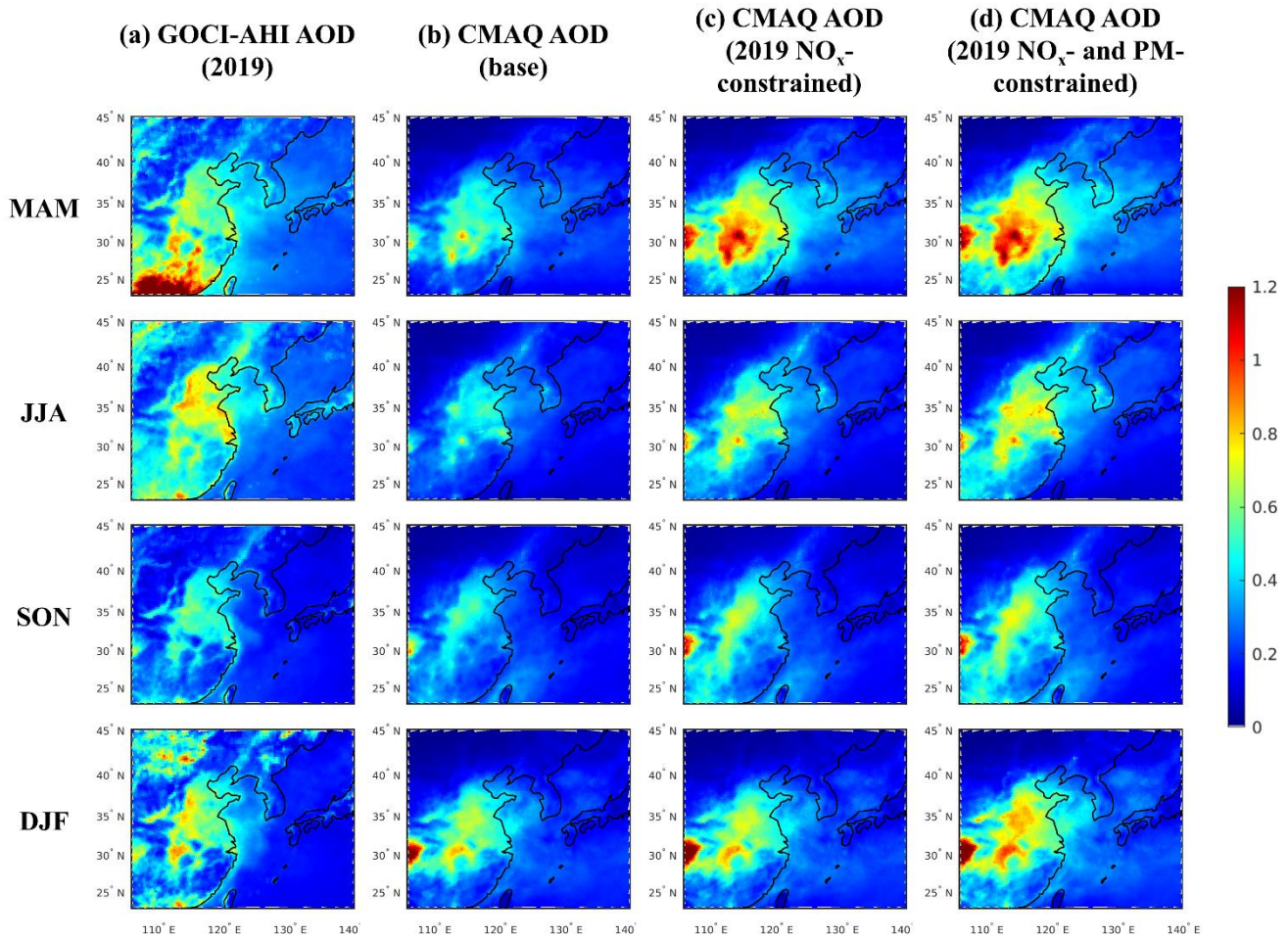
380

Figure 3. Spatial distributions of GOCI-AHI fused and CMAQ-simulated AODs before and after the NO$_x$ emissions adjustment (based on TROPOMI NO$_2$ columns) and primary PM emissions adjustment (based on GOCI-AHI AOD) during the study period 2019. (a) The GOCI-AHI AOD, (b) the CMAQ-simulated AOD using base emissions, (c) the CMAQ-simulated AOD using 2019 NO$_x$-constrained emissions, and (d) the CMAQ-simulated AOD using 2019 NO$_x$- and PM-constrained emissions. Note that CMAQ-simulated AODs were temporally collocated to the GOCI-AHI AOD.
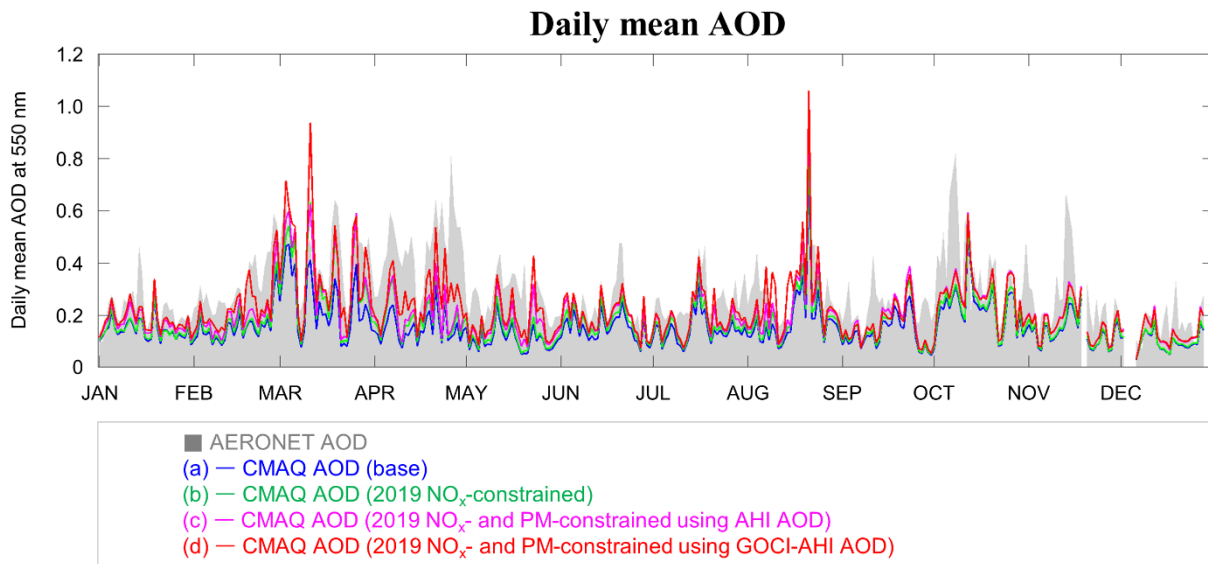
Figure 4. Comparisons of the time series of daily mean AERONET AODs (85 sites) and CMAQ-simulated daily mean AODs before and after the NO_x and primary PM emissions adjustments during the study period 2019. (a) The CMAQ-simulated AOD using the base emissions, (b) the CMAQ-simulated AOD using the 2019 NO_x-constrained emissions, (c) the CMAQ-simulated AOD using the 2019 NO_x- and PM-constrained emissions using the AHI AOD, and (d) the CMAQ-simulated AOD using the 2019 NO_x- and PM-constrained emissions using the GOCI-AHI fused AOD.

Table 1. Summary statistics of the daily mean AERONET AOD (85 sites) and the CMAQ-simulated daily mean AOD before and after the NO$_x$ emissions adjustment (based on TROPOMI NO$_2$ columns) and primary PM emissions adjustment (based on AHI AOD and GOCI-AHI AOD) during the study period 2019. (a) The CMAQ-simulated AOD using the base emissions, (b) the CMAQ-simulated AOD using 2019 NO$_x$-constrained emissions, (c) the CMAQ-simulated AOD using 2019 NO$_x$- and PM-constrained emissions using the AHI AOD, and (d) the CMAQ-simulated AOD using 2019 NO$_x$- and PM-constrained emissions using GOCI-AHI fused AOD. R: Pearson's correlation coefficient; NMB (%): normalized mean bias.

		(a) Base emissions	(b) 2019 NO$_x$-constrained emissions	2019 NO$_x$- and PM-constrained emissions	
				(c) AHI AOD	(d) GOCI-AHI AOD
MAM	R	0.45	0.43	0.45	0.45
	NMB	-64.74	-55.62	-49.63	-26.76
JJA	R	0.77	0.78	0.77	0.77
	NMB	-29.45	-19.71	-9.20	0.21
SON	R	0.57	0.57	0.62	0.62
	NMB	-51.13	-47.09	-38.03	-39.70
DJF	R	0.55	0.48	0.57	0.57
	NMB	-43.23	-41.77	-28.65	-23.36
Yearly	R	0.53	0.53	0.54	0.54
	NMB	-50.73	-42.52	-33.84	-19.60

3.2 Merits and limitations of the sequential emission adjustments and the use of the data fusion product

Despite the many top-down approaches to achieving more up-to-date emissions inventories, questions still remain about the extent to which each of the aerosol components contributes to aerosol loadings. To ascertain the possible implications for our understanding of sequential improvements in the performance of the model in simulating the AOD, we examined the chemical compositions of surface PM$_{2.5}$ in Korea during the study period 2019 on a seasonal basis. While a slightly larger portion (53.26% on average) of surface PM$_{2.5}$ loadings was comprised of secondary inorganic aerosols such as nitrate, sulfate, and ammonium aerosols (20.90%, 18.56%, and 13.81%, respectively), the total of the remaining portion (46.74% on average) was mostly comprised of primary PM and some secondary aerosols such as the organic carbon category used in this study (Table 2).

As both the contributions of primary and secondary aerosols to aerosol loadings were significant, we considered the sequential adjustments of NO$_x$ and primary PM emissions effective at improving model performance. However, setting aside the earlier improvements in the model performances achieved for the study period 2019, such a chemical makeup of PM$_{2.5}$ observed implies that the adjustment of solely NO$_x$ emissions performed in this study might not have sufficiently reduced the uncertainty underlying the emissions of the precursors of other secondary inorganic aerosols, such as sulfate and ammonium

aerosols. Considering the impending availability of the GEMS tropospheric NO$_2$ product in its mature stage, this study mainly focused on examining the utility of NO$_2$ columns, not the other gas-phase precursors, which could have been beneficial for constraining the remaining secondary inorganic aerosols. This limitation presents a need for follow-up research that employs more comprehensive sets of top-down constraints (e.g., observational references for SO$_2$ and ammonia loadings in the troposphere).

Table 2. Concentrations (μg/m^3) and compositions (%) of surface PM$_{2.5}$ and its components in Korea during the study period 2019. ANO$_3$, ASO$_4$, and ANH$_4$: nitrate, sulfate, and ammonium aerosols, respectively; OC: primary and secondary organic carbon; EC: elemental carbon; Lumped PM: the lumped summation of PM species noted in Section 2.6, Unknown: undefined PM$_{2.5}$ species noted in Section 2.6.

	ANO$_3$	ASO$_4$	ANH$_4$	OC	EC	Lumped PM	Unknown	PM$_{2.5}$
MAM	6.76 (26.02)	4.83 (18.59)	4.05 (15.59)	3.31 (12.74)	0.74 (2.84)	8.72 (17.99)	1.61 (6.22)	25.97 (100)
JJA	1.66 (10.37)	4.43 (27.68)	2.37 (14.81)	2.37 (14.83)	0.46 (2.89)	6.99 (26.01)	0.55 (3.42)	16.00 (100)
SON	2.05 (13.31)	2.43 (15.82)	1.56 (10.15)	2.56 (16.68)	0.68 (4.39)	6.27 (19.68)	3.07 (19.96)	15.38 (100)
DJF	7.34 (26.35)	4.12 (14.79)	3.79 (13.59)	3.74 (13.44)	0.95 (3.40)	9.22 (16.27)	3.39 (12.16)	27.86 (100)
Yearly	4.45 (20.90)	3.95 (18.56)	2.94 (13.81)	3.00 (14.07)	0.71 (3.31)	7.80 (19.24)	2.15 (10.12)	21.30 (100)

To account for the outperformance of the model that used the adjusted emissions based on the data fusion product, we quantified the amount of observational references available from each of the AHI AOD and GOCI-AHI AOD products. The benefit of securing more continuous and frequent observations, which provide more data available for constraining model biases, has often been highlighted in many satellite-based inverse modeling and data assimilation studies (Jeon et al., 2016; Lee et al., 2016; Yumimoto et al. 2016; Jin et al., 2019; Choi et al., 2019). We compared the numbers of valid AOD retrievals made for each of the modeling grids (hereafter referred to as AOD records) obtained from the AHI AOD and GOCI-AHI AOD products. Note that the grid-specific number of AOD records does not necessarily indicate the instrumental sampling frequency of the satellite instrument in this comparison. Whereas the AHI AOD product showed some clusters of missing values over several inland regions (i.e., southeastern and northeastern China, the Sichuan Basin, and some areas in Primorye in Russia, North Korea, and Japan), the GOCI-AHI AOD product produced more spatially complete domain-wide observations during the study period 2019 (Figure 5).

In addition to the improvement in the observational coverage, the GOCI-AHI AOD product showed a noticeable improvement in the amount of available data. Compared to the AHI AOD product, the GOCI-AHI AOD product showed increases in the numbers of AOD records by 132.23% on average during the entire study period, the seasonal extents of which ranged from 90.20% - 198.01% (Figure 5; Table 3). In other words, even though the AHI AOD and GOCI-AHI AOD were given over the modeling domain at identical spatiotemporal resolutions in the first place, there was a substantial

difference in the volume of the information available in the end. We accounted for the greater improvement in the model performance afforded by the use of GOCI-AHI AOD (Figures 3 and 4; Table 1) by the instruments supplementing undetected or discarded pixels of other instruments that originate from different aerosol retrieval algorithms and by the additional bias correction approaches (Lim et al., 2018; Choi et al., 2019; Lim et al., 2020).

445   Such an improvement in the quantity of observation references seemed to be beneficial for improving the model performance in AOD estimation. For example, in MAM 2019, the use of the emissions constrained based on GOCI-AHI AOD reduced the model bias more effectively compared to that based on AHI AOD. This improvement (or the difference in the extent of emissions adjustment) was considered to be originating from whether the high AOD peaks along southeast China were captured (Figure 3a) or not (Figure 2a). Throughout the entire year 2019, the season MAM showed the most

450   frequent occurrences of high AOD peaks over AERONET sites compared to other seasons (Figure 5). Considering the locations of those ground-based sites (Figure 1 above), many of which cover the southeast China, we first presumed that GOCI-AHI AOD would represent the aerosol loadings more realistically. And then, this was supported by the grid-specific number of AOD records afforded by AHI AOD and GOCI-AHI AOD (Figure 5), the former of which showed noticeably fewer information available for use. Therefore, we concluded that the use of the emissions constrained based on GOCI-AHI

455   AOD, which was considered to better capture the high AOD peaks across the southeast China in a spatiotemporally more frequent and continuous manner, was more effective in resolving the model's initial AOD underestimation.
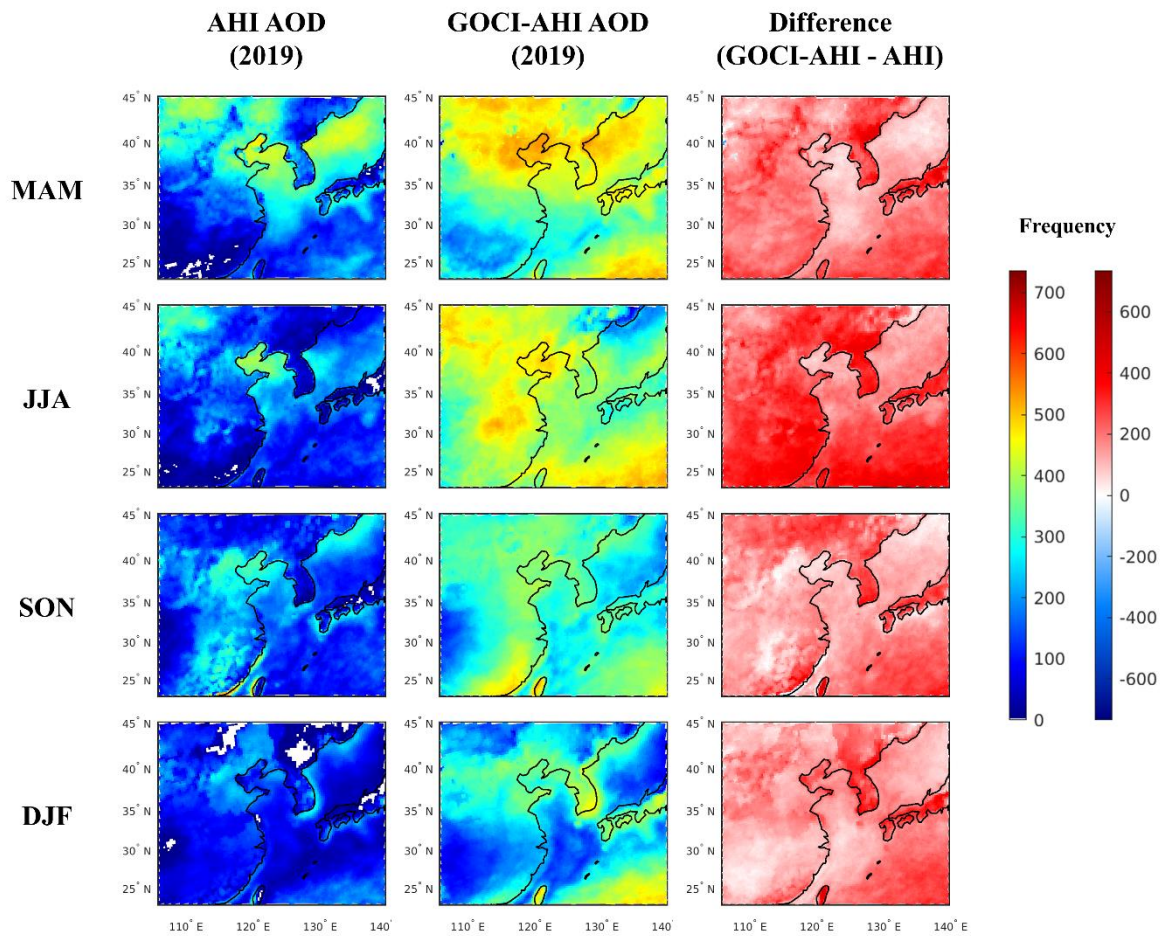
Figure 5. The number of AOD records (in each of the modeling grids) obtained from the AHI AOD product and the GOCI-AHI fused AOD product during the study period 2019.

Table 3. The number of AOD records (domain-wide) (unit: thousands) obtained from the AHI AOD product and the GOCI-AHI fused AOD product during the study period 2019.

	MAM	JJA	SON	DJF	Yearly
(a) AHI AOD	2,654	1,779	2,055	1,233	7,723
(b) GOCI-AHI AOD	5,049	5,302	4,169	3,415	17,936
Difference (b - a) (%)	90.20	198.01	102.81	176.81	132.23

3.2 Application of the top-down approach using the GEMS-AMI-GOCI-2 fused AOD product

Upon the earlier success of the use of the proxy of GEMS-AMI-GOCI-2 AOD (GOCI-AHI AOD described in Sect. 3.1) in updating the emissions inventory, which resulted in further reduced model biases compared to those from the use of the proxy of GEMS AOD (AHI AOD described in Sect. 3.1), we employed the GEMS-AMI-GOCI-2 AOD product to proceed with the emissions adjustment for the study period 2022. Note that the GOCI-AHI AOD product used earlier was served as a prototype for the development of the GEMS-AMI-GOCI-2 AOD product; the production of the GOCI-AHI AOD product has been discontinued, and it is currently only available for research purposes for the year 2019. To explore the utility of the multi-source data fusion product in constraining the temporal variations of aerosol precursor emissions and ultimately to leverage the up-to-date emissions inventory to improve model performance at simulating AOD and $PM_{2.5}$ concentrations, we used the GEMS-AMI-GOCI-2 fused AOD as top-down constraints to adjusting primary PM emissions over the modeling domain. Similar to the earlier top-down approach, we used TROPOMI NO_2 columns in advance of the primary PM emissions adjustments to constrain NO_x emissions.

Using the base emissions, the model tended to overestimate AODs over a major portion of the modeling domain, particularly across the NCP region, during the study period 2022 (Figures 6a and 6b). Upon the relative decreases in monthly mean NO_2 columns in March, April, and May 2022 compared to the corresponding months in 2019 (Figure S9), the NO_x emissions adjustment led to overall reductions in NO_x emissions by 2.83% - 13.40% (Figure S10; Table S7), which appeared to be effective at reducing the discrepancy between the observed and modeled AODs (Figure 6c). After the primary PM emission adjustment, which resulted in overall decrease in primary PM emissions by 9.03% (Figure S11; Table S8), the modeled AODs showed even closer spatial agreements with the observed AODs (Figure 6d). Then we evaluated the model performance in simulating daily mean surface $PM_{2.5}$ concentrations in Korea and the NCP region in a time-series. Similar to the earlier results shown for the study period 2019, the NO_x and primary PM emission adjustments led to overall improvements in the model performances during the study period 2022. Using the base emissions, the model overestimated $PM_{2.5}$ concentrations by 20.60% in Korea and 47.58% in the NCP region (Figure 7a; Table 4a); on the other hand, using the NO_x emission adjustment, the model reduced the extent of overestimation to 15.74% in Korea and 39.80% in the NCP region

(Figure 7b; Table 4b); and then the primary PM emission adjustment further reduced those to 6.81% and 19.58% (Figure 7c; Table 4c).

Unlike top-down constraints used during the study period 2019, those used during the study period 2022 led to overall reductions in NO_x and primary PM emissions, particularly over the highly industrialized regions (e.g., the NCP region and other major metropolitan areas in China) (Figures S10 and S11). An explanation for the noticeable decreases in NO_2 columns and AODs observed across these regions in March, April, and May 2022 compared to those observed in the corresponding months during the pre-COVID-19 period (the year 2019 in this study) (Figures 2a, 3a, 6a, and S9) was the strict city- and province-wide lockdown regulations (the so-called "zero-COVID strategy" that resumed in March 2022) (Dyer, 2022), which led to substantial reductions in the amounts of anthropogenic emissions (e.g., vehicular, industrial, and agricultural emissions) (Caporale et al., 2022) in China. In addition, the updated emissions inventory yielded more accurate representations of the aerosol loadings over the sea surface (i.e., the Yellow Sea), which could benefit other studies that involve the long-range transport of aerosols emitted from inland sources (Hatakeyama et al., 2001; Carmichael et al., 2002; Pouyaei et al., 2020, 2021; Jung et al., 2021).
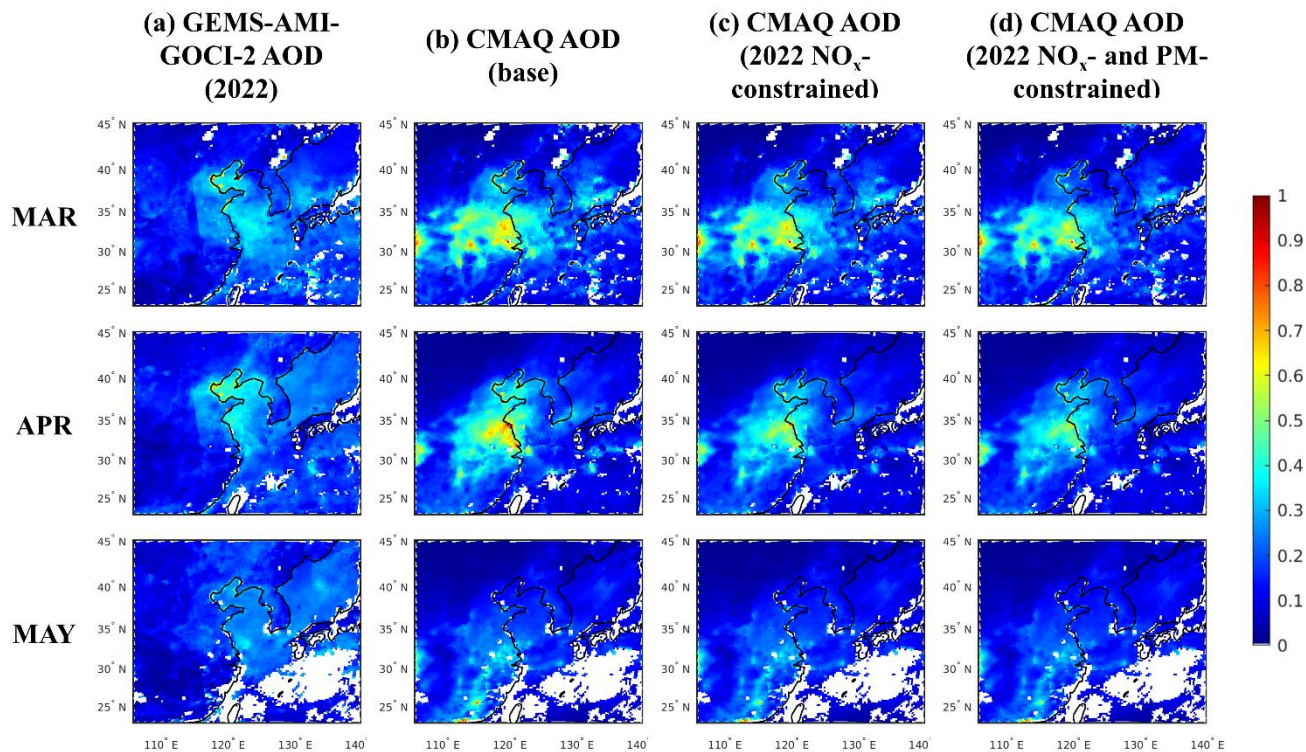
Figure 6. Spatial distributions of GEMS-AMI-GOCI-2 fused AOD and CMAQ-simulated AODs before and after the NO$_x$ and primary PM emissions adjustments during the study period 2022. (a) The GEMS-AMI-GOCI-2 AOD, (b) the CMAQ-simulated AOD using base emissions, (c) the CMAQ-simulated AOD using 2022 NO$_x$-constrained emissions, and (d) the CMAQ-simulated AOD using 2022 NO$_x$- and PM-constrained emissions.
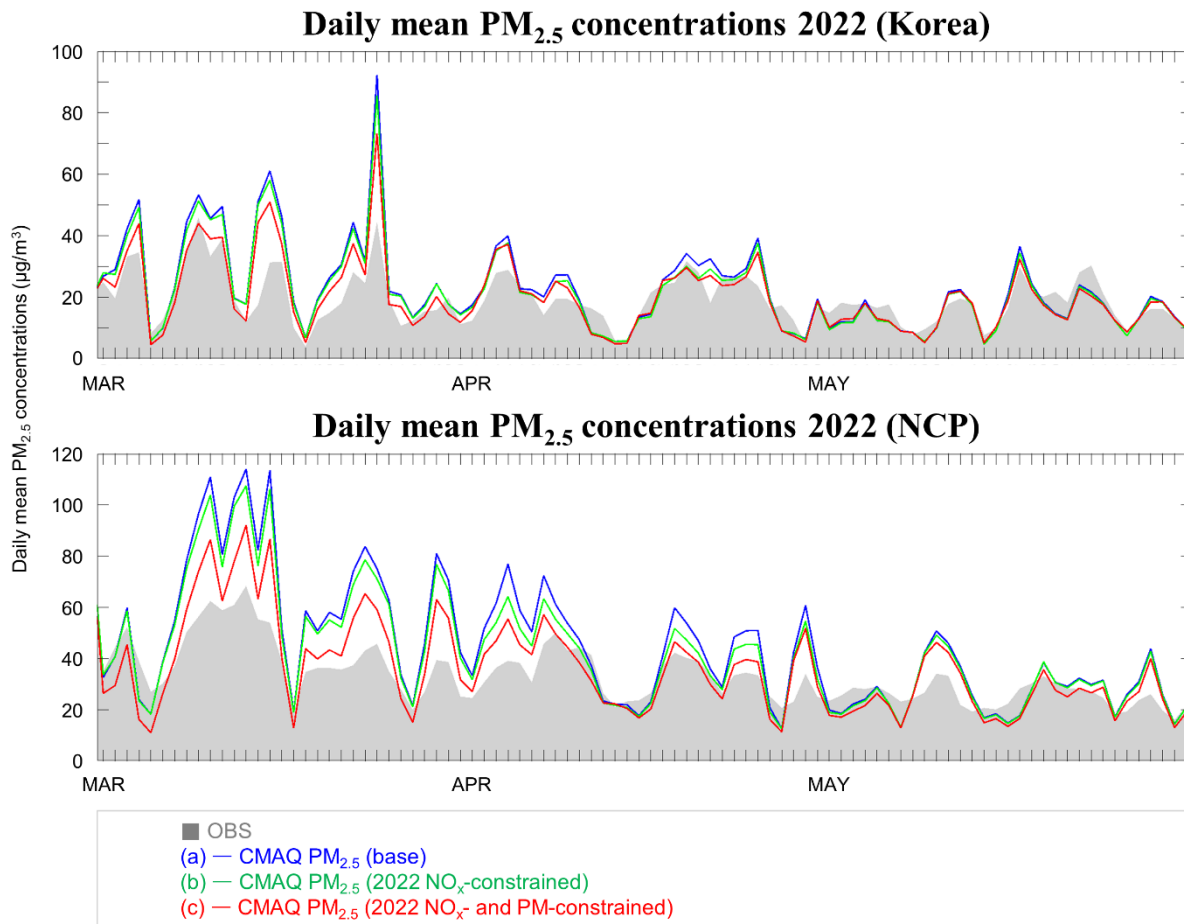
Figure 7. Comparisons of the time series of the CMAQ-simulated daily mean surface PM₂.₅ concentrations (µg/m³) before and after the NOₓ and primary PM emissions adjustments, and ground-based in situ measurements in Korea (425 sites) and the NCP region (312 sites) during the study period 2022. OBS: ground-based in situ measurements; (a) CMAQ-simulated PM₂.₅ using base emissions, (b) CMAQ-simulated PM₂.₅ using 2022 NOₓ-constrained emissions, and (c) CMAQ-simulated PM₂.₅ using 2022 NOₓ- and PM-constrained emissions.

510

515 **Table 4. Summary statistics of CMAQ-simulated daily mean PM2.5 concentrations before and after the NOx and primary PM emissions adjustments, and ground-based in situ measurements in Korea (425 sites) and the NCP region (312 sites) during the study period 2022. (a) CMAQ-simulated PM2.5 using base emissions, (b) CMAQ-simulated PM2.5 using NOx-constrained emissions, and (c) CMAQ-simulated PM2.5 using 2022 NOx- and PM-constrained emissions.**

			(a) Base emissions	(b) 2022 NOx-constrained emissions	(c) 2022 NOx- and PM-constrained emissions
Korea	MAR	R	0.81	0.81	0.81
		NMB	47.26	42.09	21.54
	APR	R	0.68	0.67	0.69
		NMB	14.67	7.83	4.25
	MAY	R	0.72	0.72	0.70
		NMB	-6.51	-8.88	-8.93
	3-month	R	0.76	0.76	0.77
		NMB	20.60	15.74	6.81
NCP	MAR	R	0.46	0.46	0.46
		NMB	73.94	65.71	32.38
	APR	R	0.41	0.42	0.41
		NMB	46.84	32.80	19.34
	MAY	R	0.31	0.31	0.30
		NMB	16.44	14.63	6.95
	3-month	R	0.50	0.50	0.48
		NMB	47.58	39.30	19.58

520 **4. Summary and Conclusion**

In summary, this study attempted to sequentially adjust bottom-up estimates of NOx and primary PM emissions over East Asia by employing observational references afforded by multiple satellite instruments retrofitted on various platforms and the synergistic science product. During the study period 2019, we reconfirmed the utility of LEO and GEO satellite products in emission adjustments and then explored that of the multi-source data fusion product, whose enhanced observational

525 quantity and quality appeared to reduce model biases in AOD simulations to a great extent. During the study period 2022, which experienced noticeable reductions in the amounts of anthropogenic emissions primarily resulting from severe lockdowns across major urban regions in China, the earlier top-down approach to constraining aerosol precursor emissions was also effective at reducing spatiotemporal discrepancies between the modeled and observed loadings of aerosols and their

precursors; particularly, the emission adjustments were effective at improving the model performances in simulating surface PM$_{2.5}$ concentrations during the lockdown period.

In light of such findings, we conclude that the series of emission adjustments in this study, which were capable of closely capturing variations in the emissions of both primary aerosols and the precursors of secondary aerosols in a top-town manner, were generally effective at improving the model performances in estimating aerosol loadings over East Asia. The enhanced observation quality and quantity afforded by the GEMS-involved synergistic product and its proxy appeared to be beneficial to capturing the spatiotemporal variations in the emissions of the aerosol precursors. In terms of possible uncertainties that could originate from other aerosol precursor species, which was outside the scope of this study, the methodology used left some room for further improvement; nonetheless, this study reconfirmed the significant association between emissions of aerosol precursors and the AOD as well as surface PM$_{2.5}$ concentrations and underscored the benefit of using multi-source, top-down information to best exploit available observational references. In light of the improvement in data availability (e.g., tropospheric SO$_2$ columns and the operational version of the data fusion product) in the near future, afforded by GEMS and its sister instruments, we conclude that the findings of this study could provide a useful basis for how to more effectively use the new data for producing more up-to-date emission inventories, the expected results of which could provide more precise insight into the spatiotemporal behaviors of air pollutants under pandemic situations.

Data availability

AHI aerosol products can be accessed at Japan Aerospace Exploration Agency Himawari Monitor (P-Tree system) database (https://www.eorc.jaxa.jp/ptree/index.html). TROPOMI tropospheric NO$_2$ columns sampled along the study area are available at European Space Agency Copernicus Services Data Hub (https://cophub.copernicus.eu/). Data fusion products may be available upon request to the authors. Ground-based in-situ measurements of NO$_2$ and PM$_{2.5}$ concentrations are available at AirKorea (https://www.airkorea.or.kr) and Chinese Ministry of Ecology and Environment (http://www.cnemc.cn/en/) databases.

Author contributions

JP took the lead in drafting the original manuscript. JP, JJ, YC, and KL set up the experimental design. JP and JJ set up the modeling system and conducted emissions adjustments and model simulations. HL, MK, YL, and JK developed and provided the multi-source data fusion products (GOCI-AHI and GEMS-AMI-GOCI-2 aerosol products). KL provided AirKorea datasets for model evaluation. YC and KL provided overall context as a principal investigator and project manager, respectively, and supervised the entire research. All authors discussed the results, exchanged comprehensive feedback on the original manuscript draft, and contributed to preparing the final version of the manuscript.

Competing interests

Some authors are members of the editorial board of the special issue (GEMS: first year in operation) jointly organized between Atmospheric Measurement Techniques and Atmospheric Chemistry and Physics. The peer-review process was guided by an independent editor, and the authors have also no other competing interests to declare.

References

570 ÅngstrÖm, A. (1961). Techniques of Determining the Turbidity of the Atmosphere. Tellus, 13(2), 214–223. https://doi.org/10.3402/tellusa.v13i2.9493

Ahn, C., Torres, O., & Jethva, H. (2014). Assessment of OMI near-UV aerosol optical depth over land. *Journal of Geophysical Research: Atmospheres*, 119(5), 2457–2473. https://doi.org/10.1002/2013JD020188.

Bellouin, N., Boucher, O., Haywood, J., & Reddy, M. S. (2005). Global estimate of aerosol direct radiative forcing from
575 satellite measurements. *Nature*, 438(7071), 1138–1141. https://doi.org/10.1038/nature04348.

Bessho, K., Date, K., Hayashi, M., Ikeda, A., Imai, T., Inoue, H., Kumagai, Y., Miyakawa, T., Murata, H., Ohno, T., Okuyama, A., Oyama, R., Sasaki, Y., Shimazu, Y., Shimoji, K., Sumida, Y., Suzuki, M., Taniguchi, H., Tsuchiyama, H., … Yoshida, R. (2016). An Introduction to Himawari-8/9—Japan's New-Generation Geostationary Meteorological Satellites. Journal of the Meteorological Society of Japan. Ser. II, 94(2), 151–183. https://doi.org/10.2151/jmsj.2016-
580 009.

Byun, D., & Schere, K. L. (2006). Review of the Governing Equations, Computational Algorithms, and Other Components of the Models-3 Community Multiscale Air Quality (CMAQ) Modeling System. *Applied Mechanics Reviews*, 59(2), 51–77. https://doi.org/10.1115/1.2128636.

Caporale, G. M., Carmona-González, N., & Gil-Alana, L. A. (2022). Atmospheric Pollution in Chinese Cities: Trends and
585 Persistence (SSRN Scholarly Paper No. 4309213). https://doi.org/10.2139/ssrn.4309213

Carmichael, G.R., Streets, D.G., Calori, G., Amann, M., Jacobson, M.Z., Hansen, J., & Ueda, H. (2002). Changing trends in sulfur emissions in Asia: Implications for acid deposition. Environ. Sci. Technol., 36, 4707-4713, doi:10.1021/es011509c.

Chan, P. K., Zhao, X.-P., & Heidinger, A. K. (2013). Long-Term Aerosol Climate Data Record Derived from Operational
590 AVHRR Satellite Observations. *Dataset Papers in Geosciences*, 2013, e140791. https://doi.org/10.7167/2013/140791.

Chen, L., Fei, Y., Wang, R., Fang, P., Han, J., & Zha, Y. (2021). Retrieval of High Temporal Resolution Aerosol Optical Depth Using the GOCI Remote Sensing Data. *Remote Sensing*, 13(12), 2376. https://doi.org/10.3390/rs13122376.

Chen, L., Mao, F., Hong, J., Zang, L., Chen, J., Zhang, Y., Gan, Y., Gong, W., & Xu, H. (2022). Improving PM2.5 predictions during COVID-19 lockdown by assimilating multi-source observations and adjusting emissions.
595 *Environmental Pollution*, 297, 118783. https://doi.org/10.1016/j.envpol.2021.118783.

Choi, M., Kim, J., Lee, J., Kim, M., Park, Y.-J., Jeong, U., Kim, W., Hong, H., Holben, B., Eck, T. F., Song, C. H., Lim, J.-H., & Song, C.-K. (2016). GOCI Yonsei Aerosol Retrieval (YAER) algorithm and validation during the DRAGON-NE Asia 2012 campaign. *Atmospheric Measurement Techniques*, 9(3), 1377–1398. https://doi.org/10.5194/amt-9-1377-2016.

600   Choi, W. J., Moon, K.-J., Yoon, J., Cho, A., Kim, S., Lee, S., Ko, D. ho, Kim, J., Ahn, M. H., Kim, D.-R., Kim, S.-M., Kim, J.-Y., Nicks, D., & Kim, J.-S. (2018). Introducing the geostationary environment monitoring spectrometer. *Journal of Applied Remote Sensing*, 12(4), 044005. https://doi.org/10.1117/1.JRS.12.044005.

Choi, M., Kim, J., Lee, J., Kim, M., Park, Y.-J., Holben, B., Eck, T. F., Li, Z., & Song, C. H. (2018). GOCI Yonsei aerosol retrieval version 2 products: An improved algorithm and error analysis with uncertainty estimation from 5-year

605   validation over East Asia. *Atmospheric Measurement Techniques*, 11(1), 385–408. https://doi.org/10.5194/amt-11-385-2018.

Choi, M., Lim, H., Kim, J., Lee, S., Eck, T. F., Holben, B. N., Garay, M. J., Hyer, E. J., Saide, P. E., & Liu, H. (2019). Validation, comparison, and integration of GOCI, AHI, MODIS, MISR, and VIIRS aerosol optical depth over East Asia during the 2016 KORUS-AQ campaign. *Atmospheric Measurement Techniques*, 12(8), 4619–4641.

610   https://doi.org/10.5194/amt-12-4619-2019.

Chung, S.-R., Ahn, M.-H., Han, K.-S., Lee, K.-T., & Shin, D.-B. (2020). Meteorological Products of Geo-KOMPSAT 2A (GK2A) Satellite. *Asia-Pacific Journal of Atmospheric Sciences*, 56(2), 185–185. https://doi.org/10.1007/s13143-020-00199-x.

Cooper, M., Martin, R. V., Padmanabhan, A., & Henze, D. K. (2017). Comparing mass balance and adjoint methods for

615   inverse modeling of nitrogen dioxide columns for global nitrogen oxide emissions. *Journal of Geophysical Research: Atmospheres*, 122(8), 4718–4734. https://doi.org/10.1002/2016JD025985.

Dyer, O. (2022). Covid-19: Lockdowns spread in China as omicron tests "zero covid" strategy. *BMJ*, 376, o859. https://doi.org/10.1136/bmj.o859.

Filonchyk, M., Yan, H., Zhang, Z., Yang, S., Li, W., & Li, Y. (2019). Combined use of satellite and surface observations to

620   study aerosol optical depth in different regions of China. *Scientific Reports*, 9(1), 6174. https://doi.org/10.1038/s41598-019-42466-6.

Garay, M. J., Witek, M. L., Kahn, R. A., Seidel, F. C., Limbacher, J. A., Bull, M. A., Diner, D. J., Hansen, E. G., Kalashnikova, O. V., Lee, H., Nastan, A. M., & Yu, Y. (2020). Introducing the 4.4 km spatial resolution Multi-Angle Imaging SpectroRadiometer (MISR) aerosol product. *Atmospheric Measurement Techniques*, 13(2), 593–628.

625   https://doi.org/10.5194/amt-13-593-2020.

Guenther, A.B., Karl, T., Harley, P., Wiedinmyer, C., Palmer, P. I., & Geron, C. (2006). Estimates of global terrestrial isoprene emissions using MEGAN (Model of Emissions of Gases and Aerosols from Nature). *Atmospheric Chemistry and Physics*, 6(11), 3181–3210. https://doi.org/10.5194/acp-6-3181-2006.

Guenther, A. B., Jiang, X., Heald, C. L., Sakulyanontvittaya, T., Duhl, T., Emmons, L. K., & Wang, X. (2012). The Model

630   of Emissions of Gases and Aerosols from Nature version 2.1 (MEGAN2.1): An extended and updated framework for modeling biogenic emissions. *Geoscientific Model Development*, 5(6), 1471–1492. https://doi.org/10.5194/gmd-5-1471-2012.

Guenther, A., Jiang, X., Shah, T., Huang, L., Kemball-Cook, S., & Yarwood, G. (2020). Model of Emissions of Gases and Aerosol from Nature Version 3 (MEGAN3) for Estimating Biogenic Emissions. In C. Mensink, W. Gong, & A. Hakami (Eds.), Air Pollution Modeling and its Application XXVI (pp. 187–192). *Springer International Publishing*. https://doi.org/10.1007/978-3-030-22055-6_29

Go, S., Kim, J., Park, S. S., Kim, M., Lim, H., Kim, J.-Y., Lee, D.-W., & Im, J. (2020). Synergistic Use of Hyperspectral UV-Visible OMI and Broadband Meteorological Imager MODIS Data for a Merged Aerosol Product. *Remote Sensing*, 12(23), Article 23. https://doi.org/10.3390/rs12233987.

Hatakeyama, S., Murano, K., Sakamaki, F., Mukai, H., Bandow, H., & Komazaki, Y. (2001). Transport of Atmospheric Pollutants from East Asia. *Water, Air, and Soil Pollution*, 130(1), 373–378. https://doi.org/10.1023/A:1013877000169.

Holben, B. N., Eck, T. F., Slutsker, I., Tanr´e, D., Buis, J. P., Setzer, A., Vermote, E., Reagan, J. A., Kaufmann, Y. J., Nakajima, T., Lavenu, F., Jankowiak, I., & Smirnov, A. (1998). AERONET: A federated instrument network and data archive for aerosol characterisation, *Remote Sens. Environ.*, 66, 1–16.

Ingmann, P., Veihelmann, B., Langen, J., Lamarre, D., Stark, H., & Courrèges-Lacoste, G. B. (2012). Requirements for the GMES Atmosphere Service and ESA's implementation concept: Sentinels-4/-5 and -5p. *Remote Sensing of Environment*, 120, 58–69. https://doi.org/10.1016/j.rse.2012.01.023.

Jang, Y., Lee, Y., Kim, J., Kim, Y., Woo, J.-H. (2019). Improvement China Point Source for Improving Bottom-Up Emission Inventory. *Asia Pac. J. Atmos. Sci.*, 56, 107–118.

Jeon, W., Choi, Y., Percell, P., Souri, A. H., Song, C.-K., Kim, S.-T., & Kim, J. (2016). Computationally efficient air quality forecasting tool: Implementation of STOPS v1.5 model into CMAQ v5.0.2 for a prediction of Asian dust. *Geoscientific Model Development*, 9(10), 3671–3684. https://doi.org/10.5194/gmd-9-3671-2016.

Jiang, Z., Vargas, M., & Csiszar, I. (2016). New oprational real-time daily rolling weekly Green Vegetation fraction product derived from suomi NPP VIIRS reflectance data. 2016 IEEE International Geoscience and Remote Sensing Symposium (IGARSS), 3524–3527. https://doi.org/10.1109/IGARSS.2016.7729911.

Jin, J., Segers, A., Heemink, A., Yoshida, M., Han, W., & Lin, H.-X. (2019). Dust Emission Inversion Using Himawari-8 AODs Over East Asia: An Extreme Dust Event in May 2017. *Journal of Advances in Modeling Earth Systems*, 11(2), 446–467. https://doi.org/10.1029/2018MS001491.

Jung, J., Souri, A. H., Wong, D. C., Lee, S., Jeon, W., Kim, J., & Choi, Y. (2019). The Impact of the Direct Effect of Aerosols on Meteorology and Air Quality Using Aerosol Optical Depth Assimilation During the KORUS-AQ Campaign. *Journal of Geophysical Research: Atmospheres*, 124(14), 8303–8319. https://doi.org/10.1029/2019JD030641.

Jung, J., Choi, Y., Wong, D. C., Nelson, D., & Lee, S. (2021). Role of Sea Fog Over the Yellow Sea on Air Quality With the Direct Effect of Aerosols. *Journal of Geophysical Research: Atmospheres*, 126(5), e2020JD033498. https://doi.org/10.1029/2020JD033498.

Jung, J., Choi, Y., Souri, A. H., Mousavinezhad, S., Sayeed, A., & Lee, K. (2022). The Impact of Springtime-Transported Air Pollutants on Local Air Quality With Satellite-Constrained NOx Emission Adjustments Over East Asia. *Journal of Geophysical Research: Atmospheres*, 127(5), e2021JD035251. https://doi.org/10.1029/2021JD035251.

Kim, J., Choi, M., Kim, M., Lim, H., Lee, S., Moon, K. J., Choi, W. J., Yoon, J. M., Kim, S.-K., Ko, D. H., Lee, S. H., Park, Y., & Chung, C.-Y. (2018). Monitoring Atmospheric Composition by Geo-Kompsat-2: Goci-2, Ami and Gems. IGARSS 2018 - 2018 IEEE International Geoscience and Remote Sensing Symposium, 7750–7752. https://doi.org/10.1109/IGARSS.2018.8518713.

Kim, J., Jeong, U., Ahn, M.-H., Kim, J. H., Park, R. J., Lee, H., Song, C. H., Choi, Y.-S., Lee, K.-H., Yoo, J.-M., Jeong, M.-J., Park, S. K., Lee, K.-M., Song, C.-K., Kim, S.-W., Kim, Y. J., Kim, S.-W., Kim, M., Go, S., … Choi, Y. (2020a). New Era of Air Quality Monitoring from Space: Geostationary Environment Monitoring Spectrometer (GEMS). Bulletin of the American Meteorological Society, 101(1), E1–E22. https://doi.org/10.1175/BAMS-D-18-0013.1.

Kim, M., Kim, J., Lim, H., & Chan, P. W. (2020b). The implementation of Yonsei Aerosol Retrieval (YAER) Algorithm to GK-2A/AMI and FY-4A/AGRI. American Geophysical Union, Fall Meeting 2020, A141-0007.

Kim, D., Gu, M., Oh, T.-H., Kim, E.-K., & Yang, H.-J. (2021). Introduction of the Advanced Meteorological Imager of Geo-Kompsat-2a: In-Orbit Tests and Performance Validation. *Remote Sensing*, 13(7), Article 7. https://doi.org/10.3390/rs13071303.

Koo, Y.-S., Choi, D.-R., Kwon, H.-Y., Jang, Y.-K., & Han, J.-S. (2015). Improvement of PM_{10} prediction in East Asia using inverse modeling. *Atmospheric Environment*, 106, 318–328. https://doi.org/10.1016/j.atmosenv.2015.02.004.

Ku, B., & Park, R. J. (2013). Comparative inverse analysis of satellite (MODIS) and ground (PM_{10}) observations to estimate dust emissions in East Asia. *Asia-Pacific Journal of Atmospheric Sciences*, 49(1), 3–17. https://doi.org/10.1007/s13143-013-0002-5.

Kumar, N., Chu, A., & Foster, A. (2007). An empirical relationship between $PM_{2.5}$ and aerosol optical depth in Delhi Metropolitan. *Atmospheric Environment*, 41(21), 4492–4503. https://doi.org/10.1016/j.atmosenv.2007.01.046.

Lee, S., Song, C. H., Park, R. S., Park, M. E., Han, K. M., Kim, J., et al. (2016). GIST-PM-Asia v1: Development of a numerical system to improve particulate matter forecasts in South Korea using geostationary satellite-retrieved aerosol optical data over Northeast Asia. *Geoscientific Model Development*, 9(1), 17–39. https://doi.org/10.5194/gmd-9-17-2016.

Lee, K., Kim, M., Choi, M., Kim, K., Choi, Y., Jeong, J., Moon, K-J., & Lee, S. (2022). Fast and operational gap filling in satellite-derived aerosol optical depths using statistical techniques. *J. Appl. Rem. Sens*, 16(4). https://doi.org/10.1117/1.JRS.16.044507.

Lee, S., Song, C. H., Han, K. M., Henze, D. K., Lee, K., Yu, J., Woo, J.-H., Jung, J., Choi, Y., Saide, P. E., & Carmichael, G. R. (2022). Impacts of uncertainties in emissions on aerosol data assimilation and short-term $PM_{2.5}$ predictions over Northeast Asia. *Atmospheric Environment*, 271, 118921. https://doi.org/10.1016/j.atmosenv.2021.118921.

Levy, R. C., Mattoo, S., Munchak, L. A., Remer, L. A., Sayer, A. M., Patadia, F., & Hsu, N. C. (2013). The Collection 6 MODIS aerosol products over land and ocean. *Atmospheric Measurement Techniques*, 6(11), 2989–3034. https://doi.org/10.5194/amt-6-2989-2013.

Levy, R., Hsu, C., et al. (2015). MODIS Atmosphere L2 Aerosol Product. NASA MODIS Adaptive Processing System, Goddard Space Flight Center, USA. http://dx.doi.org/10.5067/MODIS/MOD04_L2.006.

Li, N., Tang, K., Wang, Y., Wang, J., Feng, W., Zhang, H., Liao, H., Hu, J., Long, X., Shi, C., & Su, X. (2021). Is the efficacy of satellite-based inversion of SO_2 emission model dependent? *Environmental Research Letters*, 16(3), 035018. https://doi.org/10.1088/1748-9326/abe829.

Li, K., Ni, R., Jiang, T., Tian, Y., Zhang, X., Li, C., & Xie, C. (2022). The regional impact of the COVID-19 lockdown on the air quality in Ji'nan, China. *Scientific Reports*, 12(1), Article 1. https://doi.org/10.1038/s41598-022-16105-6.

Lim, H., Go, S., Kim, J., Choi, M., Lee, S., Song, C.-K., & Kasai, Y. (2021). Integration of GOCI and AHI Yonsei aerosol optical depth products during the 2016 KORUS-AQ and 2018 EMeRGe campaigns. *Atmospheric Measurement Techniques*, 14(6), 4575–4592. https://doi.org/10.5194/amt-14-4575-2021.

Lim, H., Choi, M., Kim, J., Kasai, Y., & Chan, P. W. (2018). AHI/Himawari-8 Yonsei Aerosol Retrieval (YAER): Algorithm, Validation and Merged Products. *Remote Sensing*, 10(5), 699. https://doi.org/10.3390/rs10050699.

Martin, R. V., Jacob, D. J., Chance, K., Kurosu, T. P., Palmer, P. I., & Evans, M. J. (2003). Global inventory of nitrogen oxide emissions constrained by space-based observations of NO_2 columns. *Journal of Geophysical Research: Atmospheres*, 108(D17). https://doi.org/10.1029/2003JD003453

Mousavinezhad, S., Choi, Y., Pouyaei, A., Ghahremanloo, M., & Nelson, D. L. (2021). A comprehensive investigation of surface ozone pollution in China, 2015–2019: Separating the contributions from meteorology and precursor emissions. *Atmospheric Research*, 257, 105599. https://doi.org/10.1016/j.atmosres.2021.105599.

Munchak, L. A., Levy, R. C., Mattoo, S., Remer, L. A., Holben, B. N., Schafer, J. S., Hostetler, C. A., & Ferrare, R. A. (2013). MODIS 3 km aerosol product: Applications over land in an urban/suburban region. *Atmospheric Measurement Techniques*, 6(7), 1747–1759. https://doi.org/10.5194/amt-6-1747-2013.

Napelenok, S. L., Cohan, D. S., Hu, Y., & Russell, A. G. (2006). Decoupled direct 3D sensitivity analysis for particulate matter (DDM-3D/PM). *Atmospheric Environment*, 40(32), 6112–6121. https://doi.org/10.1016/j.atmosenv.2006.05.039.

Ohara, T., Akimoto, H., Kurokawa, J., Horii, N., Yamaji, K., Yan, X., & Hayasaka, T. (2007). An Asian emission inventory of anthropogenic emission sources for the period 1980-2020. *Atmospheric Chemistry and Physics*, 7(16), 4419–4444. https://doi.org/10.5194/acp-7-4419-2007.

Okuyama, A., Andou, A., Date, K., Hoasaka, K., Mori, N., Murata, H., Tabata, T., Takahashi, M., Yoshino, R., & Bessho, K. (2015). Preliminary validation of Himawari-8/AHI navigation and calibration. *Earth Observing Systems*, 9607, 663–672. https://doi.org/10.1117/12.2188978.

Pang, J., Liu, Z., Wang, X., Bresch, J., Ban, J., Chen, D., & Kim, J. (2018). Assimilating AOD retrievals from GOCI and VIIRS to forecast surface PM2.5 episodes over Eastern China. *Atmospheric Environment*, 179, 288–304. https://doi.org/10.1016/j.atmosenv.2018.02.011.

Park, J., Jung, J., Choi, Y., Mousavinezhad, S., & Pouyaei, A. (2022). The sensitivities of ozone and $PM_{2.5}$ concentrations to the satellite-derived leaf area index over East Asia and its neighboring seas in the WRF-CMAQ modeling system. *Environmental Pollution*, 306, 119419. https://doi.org/10.1016/j.envpol.2022.119419.

Pitchford, M., Maim, W., Schichtel, B., Kumar, N., Lowenthal, D., & Hand, J. (2007). Revised algorithm for estimating light extinction from IMPROVE particle speciation data. *Journal of the Air & Waste Management Association* 57(11), 1326–1336. https://doi.org/10.3155/1047-3289.57.11.1326.

Pouyaei, A., Choi, Y., Jung, J., Sadeghi, B., & Song, C. H. (2020). Concentration Trajectory Route of Air pollution with an Integrated Lagrangian model (C-TRAIL Model v1.0) derived from the Community Multiscale Air Quality Model (CMAQ Model v5.2). *Geoscientific Model Development*, 13(8), 3489–3505. https://doi.org/10.5194/gmd-13-3489-2020.

Pouyaei, A., Sadeghi, B., Choi, Y., Jung, J., Souri, A. H., Zhao, C., & Song, C. H. (2021). Development and Implementation of a Physics-Based Convective Mixing Scheme in the Community Multiscale Air Quality Modeling Framework. *Journal of Advances in Modeling Earth Systems*, 13(6), e2021MS002475. https://doi.org/10.1029/2021MS002475.

Remer, L. A., Mattoo, S., Levy, R. C., & Munchak, L. A. (2013). MODIS 3 km aerosol product: Algorithm and global perspective. *Atmospheric Measurement Techniques*, 6(7), 1829–1844. https://doi.org/10.5194/amt-6-1829-2013.

Remer, L. A., Kleidman, R. G., Levy, R. C., Kaufman, Y. J., Tanré, D., Mattoo, S., Martins, J. V., Ichoku, C., Koren, I., Yu, H., & Holben, B. N. (2008). Global aerosol climatology from the MODIS satellite sensors. *Journal of Geophysical Research: Atmospheres*, 113(D14). https://doi.org/10.1029/2007JD009661.

Rodgers, C.D. (2000). Inverse Methods for Atmospheric Sounding: Theory and Practice, Series on Atmospheric, Oceanic and Planetary Physics. *WORLD SCIENTIFIC*. https://doi.org/10.1142/3171.

Skamarock, W. C., Klemp, J. B., Dudhia, J., Gill, D. O., Barker, D., Duda, M. G., … Powers, J. G. (2008). A Description of the Advanced Research WRF Version 3 (No. NCAR/TN-475+STR). University Corporation for Atmospheric Research. https://doi.org/10.5065/D68S4MVH.

Souri, A. H., Nowlan, C. R., González Abad, G., Zhu, L., Blake, D. R., Fried, A., Weinheimer, A. J., Wisthaler, A., Woo, J.-H., Zhang, Q., Chan Miller, C. E., Liu, X., & Chance, K. (2020). An inversion of NO_x and non-methane volatile organic compound (NMVOC) emissions using satellite observations during the KORUS-AQ campaign and implications for surface ozone over East Asia. *Atmospheric Chemistry and Physics*, 20(16), 9837–9854. https://doi.org/10.5194/acp-20-9837-2020.

Tian, J. & Chen, D. (2010). Spectral, spatial, and temporal sensitivity of correlating MODIS aerosol optical depth with ground-based fine particulate matter ($PM_{2.5}$) across southern Ontario. *Canadian Journal of Remote Sensing*, 36, 119-128. 10.5589/m10-033.

Toon, O. B., et al. (2016), Planning, implementation and scientific goals of the Studies of Emissions and Atmospheric Composition, Clouds and Climate Coupling by Regional Surveys (SEAC4RS) field mission, *J. Geophys. Res. Atmos.*, 121, 4967–5009, doi:10.1002/2015JD024297.

Veefkind, J. P., Aben, I., McMullan, K., Förster, H., de Vries, J., Otter, G., Claas, J., Eskes, H. J., de Haan, J. F., Kleipool, Q., van Weele, M., Hasekamp, O., Hoogeveen, R., Landgraf, J., Snel, R., Tol, P., Ingmann, P., Voors, R., Kruizinga, B., … Levelt, P. F. (2012). TROPOMI on the ESA Sentinel-5 Precursor: A GMES mission for global observations of the atmospheric composition for climate, air quality and ozone layer applications. *Remote Sensing of Environment*, 120, 70–83. https://doi.org/10.1016/j.rse.2011.09.02.

Vijayaraghavan, K., Snell, H. E., & Seigneur, C. (2008). Practical Aspects of Using Satellite Data in Air Quality Modeling. *Environmental Science & Technology*, 42(22), 8187–8192. https://doi.org/10.1021/es7031339.

Wang, J., Xu, X., Henze, D. K., Zeng, J., Ji, Q., Tsay, S.-C., & Huang, J. (2012). Top-down estimate of dust emissions through integration of MODIS and MISR aerosol retrievals with the GEOS-Chem adjoint model. *Geophysical Research Letters*, 39(8). https://doi.org/10.1029/2012GL051136.

Wang, Y., Wang, J., Xu, X., Henze, D. K., Qu, Z., & Yang, K. (2020). Inverse modeling of SO_2 and NO_x emissions over China using multisensor satellite data – Part 1: Formulation and sensitivity analysis. *Atmospheric Chemistry and Physics*, 20(11), 6631–6650. https://doi.org/10.5194/acp-20-6631-2020.

Woo, J.-H., Kim, Y., Kim, H.-K., Choi, K.-C., Eum, J.-H., Lee, J.-B., Lim, J.-H., Kim, J., & Seong, M. (2020). Development of the CREATE Inventory in Support of Integrated Climate and Air Quality Modeling for Asia. *Sustainability*, 12(19), 7930. https://doi.org/10.3390/su12197930.

Xia, X., Min, J., Shen, F., Wang, Y., & Yang, C. (2019). Aerosol Data Assimilation Using Data from Fengyun-3A and MODIS: Application to a Dust Storm over East Asia in 2011. *Advances in Atmospheric Sciences*, 36(1), 1–14. https://doi.org/10.1007/s00376-018-8075-9.

Yeo, S.Y., Lee, H.K., Choi, S.W, Seol, S.H., Jin, H.A., Yoo, C., Lim, J.Y., Kim, J.S. (2019). Analysis of the national air pollutant emission inventory (CAPSS 2015) and the major cause of change in Republic of Korea. *Asian J. Atmos. Environ.* 13 (3), 212–231. https://doi.org/10.5572/ajae.2019.13.3.212.

Yuan, H., Dai, Y., Xiao, Z., Ji, D., & Shangguan, W. (2011). Reprocessing the MODIS Leaf Area Index products for land surface and climate modelling. *Remote Sensing of Environment*, 115(5), 1171–1187. https://doi.org/10.1016/j.rse.2011.01.001.

Yumimoto, K., Nagao, T. m., Kikuchi, M., Sekiyama, T. t, Murakami, H., Tanaka, T. y., Ogi, A., Irie, H., Khatri, P., Okumura, H., Arai, K., Morino, I., Uchino, O., & Maki, T. (2016). Aerosol data assimilation using data from Himawari-8, a next-generation geostationary meteorological satellite. *Geophysical Research Letters*, 43(11), 5886–5894. https://doi.org/10.1002/2016GL069298.

Zhang, W., Xu, H., & Zheng, F. (2018). Aerosol Optical Depth Retrieval over East Asia Using Himawari-8/AHI Data. *Remote Sensing*, 10(1), 137. https://doi.org/10.3390/rs10010137.

Zoogman, P., and Coauthors, 2011: Ozone air quality measurement requirements for a geostationary satellite mission. *Atmos. Environ.*, 45, 7143–7150, https://doi.org/10.1016/j.atmosenv.2011.05.058.

Zou, B., Liu, N., Wang, W., Feng, H., Liu, X., & Lin, Y. (2020). An Effective and Efficient Enhanced Fixed Rank Smoothing Method for the Spatiotemporal Fusion of Multiple-Satellite Aerosol Optical Depth Products. *Remote Sensing*, 12(7), Article 7. https://doi.org/10.3390/rs12071102.